Imaging the Earth using Time-domain Surface-wave Measurements: Evaluation and Correction of the Finite-frequency Phase Shift

Yihe Xu[1,2], Sergei Lebedev[1,2], Thomas Meier[3]

[1]Department of Earth Sciences, Bullard Laboratories, University of Cambridge, Cambridge, United Kingdom.

[2]Geophysics Section, School of Cosmic Physics, Dublin Institute for Advanced Studies, Dublin, Ireland.

[3]Institute of Geophysics, Christian-Albrechts University Kiel, Kiel, Germany.

Corresponding author: Yihe Xu (yx362@cam.ac.uk)

Key Points:

- We identify a source of errors that can cause up to ~1% error in surface-wave phase-velocity measurements.
- The error applies to all the time-domain methods that use bandpass-filtered waveforms.
- We derive an explicit formula to evaluate the error and provide a numerical method to compute and remove it.

Abstract

Surface waves propagating from earthquakes, active sources or within the ambient noise wavefield are widely used to image Earth structure at various scales, from centimeters to hundreds of kilometers. The accuracy of surface-wave, phase-velocity measurements is essential for the accuracy of the Earth models they constrain. Here, we identify a finite-frequency phase shift in the phase travel time that causes systematic errors in time-domain, phase-velocity measurements. The phase shift arises from the approximation of monochromatic surface waves with narrow-band filtered surface waves. We derive an explicit formula of the finite-frequency phase shift and present a numerical method for its evaluation and for the correction of the measurements. Applications to high-frequency and long-period examples show that the phase shift is typically around $\pi/60$-$\pi/16$ for the common settings of ambient-noise imaging studies, which translates to 0.2-0.8% phase-velocity measurement errors. The finite-frequency phase shift depends on the (1) second derivative of the wavenumber with respect to frequency; (2) width of the narrow-band filter; (3) epicentral or interstation distance; (4) center frequency of the filter. In conversion to phase velocity, the last two factors cancel out. Frequency-domain methods for phase-velocity measurements have the advantage of not producing the finite-frequency phase shift. Both time- and frequency-domain measurements, however, can be impacted by a break-down of the far-field approximation (near-field phase shift), which our calculations also show. Our method offers an effective means of improving the accuracy of the widely used time-domain, phase-velocity measurements via the evaluation of and corrections for the finite-frequency phase shift.

Plain Language Summary

Surface waves sample the 'surface layer' of the Earth with the thickness of the layer depending on the wave's wavelength. Combining surface waves of different wavelengths, or different frequencies, can provide a detailed image of the Earth's structure over a large depth range. Measuring the velocity at which surface waves travel is a crucial step in this process. In this study, we identify a source of errors in the measurements that has not received much notice so far. We first derive a formula for the possible bias and then develop a numerical method to evaluate and correct it. Applications of the numerical method reveal the effects of the bias in two common scenarios, in the surface-wave studies of the shallow (kilometers deep) and deep (hundreds of kilometers deep) structure of the Earth. Our results provide a means to improve the accuracy of the surface wave measurements and, thus, the accuracy of the surface-wave imaging of the Earth.

1 Introduction

Surface waves sample the Earth's interior at scales from centimeters to hundreds of kilometers, with varying resolution depending on their frequency. Intermediate- and long-period (>5 s) surface waves generated by earthquakes provide essential constraints on the shear-wave velocity structure and anisotropy of the crust (e.g., Agius & Lebedev, 2014, 2017; Bourjot & Romanowicz 1992; Levshin & Ratnikova, 1984; U. Meier et al. 2007; Polat et al. 2012; Press & Ewing, 1955), lithosphere and asthenosphere (e.g., Bonadio et al. 2021; Deschamps et al. 2008; Ekström & Dziewonski 1998; El-Sharkawy 2020; Masters et al. 1996; T. Meier et al. 2004; Pasyanos et al. 2014; Shapiro & Ritzwoller 2002; Zhang et al. 2009), and crustal and upper-mantle interfaces (e.g., Bartzsch et al. 2011; Beghein et al. 2019; Lebedev et al., 2013). High-frequency (>5 Hz) surface waves generated by active sources have been used to constrain upper-crustal and near-surface structure (e.g., Mi et al. 2020; Pan et al., 2019; Socco et al., 2010; Wathelet et al.,

2004; Xia et al., 1999). Ultrasonic (>20 kHz) surface waves image the top few centimeters beneath the surface, providing information about hidden cracks in concrete and weathering in historical sites (e.g., Aggelis et al., 2010; Bodet et al. 2005; T. Meier et al., 2017).

During the last two decades, ambient noise interferometry (cross-correlation of noise recorded at two receivers yielding estimates of the Green's functions) has been widely adopted as an additional approach for surface-wave imaging. It provides abundant surface wave observations and fills the frequency gap between earthquakes and active sources. It also facilitates the imaging of regions where earthquakes and active sources cannot provide sufficient illumination (e.g., Li et al., 2016; Mordret et al., 2013; Nicolson et al., 2014; Zhan et al., 2014). Ambient noise surface wave tomography has been successfully applied to imaging subsurface structure and anisotropy from the crustal and upper mantle scale (e.g., Moschetti et al., 2007; Pawlak et al. 2012; Sabra et al., 2005; Shapiro et al., 2005; Yao et al., 2006), to the scale of a basin, a volcano, or a fault region (e.g., Brenguier et al., 2007; Delorey & Vidale, 2011; Inzunza et al., 2019; Martins et al., 2019; Mordret et al., 2019; Roux et al., 2011), and to a mineral-deposit scale (e.g., Bellefleur et al., 2015; Hollis et al., 2019; Mordret et al., 2013; Xu et al., 2021). The method is also applied in other fields, such as cryoseismology (e.g., Lindner et al., 2019; Preiswerk & Walter, 2018).

Accurate group or phase velocity measurements are the foundation of most surface-wave studies at any scale. The measurement methods fall into two categories, with the measurements performed either in the time domain or in the frequency domain. Time-domain methods measure the arrival time or the instantaneous phase of surface waves in the time domain and then convert them to the velocity. One representative method is the frequency-time analysis (FTAN; Bensen et al., 2007; Dziewonski et al., 1969; Dziewonski & Bloch, 1972; Ritzwoller & Levshin, 1998; Yao et al., 2006). Using a set of narrow-band filters, the original, broadband surface waves are turned

into a set of narrow-band surface-wave signals. One can then measure the phase travel time or instantaneous phase on the narrow-band seismograms to obtain phase velocities, or measure the group travel time on the envelopes to obtain group velocities. Using multiple stations can solve the ambiguity in the phase velocity measurement (e.g., Martins et al., 2019; Xia et al., 1999), even determine the direction of phase velocity (e.g., Kolínský et al., 2019).

The time-domain methods for the determination of the phase velocity implicitly assume that the narrow-band signals represent the monochromatic surface waves at the center frequencies of the filters. The approximation can result in systematic errors in the measurements. By contrast, frequency-domain methods measure the phase of the spectra using the Fourier transform (Bonadio et al., 2018, 2021; Fry et al., 2010; Kästle et al., 2016; T. Meier et al., 2004; Molinari et al., 2015; Verbeke et al., 2012; Zhang et al. 2007). The frequency-domain methods do not rely on the assumption of monochromaticity of narrow-band surface waves. However, they require effective procedures for identifying the correct 2π branch of the phase of the surface wave (e.g. Bonadio et al., 2018, 2021; Soomro et al., 2016).

Both the time- and frequency-domain methods, originally developed for earthquake seismograms, have been applied in ambient noise studies with minor modifications. The difference is that the initial phase of virtual sources is zero (Bensen et al., 2007; Bonadio, 2019; Kästle et al., 2016; Yao et al., 2006), as the cross-correlation in noise interferometry cancels out the original initial phase from noise sources. Moreover, the zero initial phase leads to an alternative frequency-domain method as well (Aki, 1957; Ekström, 2014; Ekström et al., 2009). The spectrum of the noise cross-correlation functions (NCFs) is found to resemble a Bessel function with the argument of $\omega\Delta/c(\omega)$, where ω is angular frequency, Δ is interstation distance and c—phase velocity. Phase velocity can be obtained by fitting the Bessel function to the real part of the spectrum of NCFs.

In this paper, we focus on the accuracy of phase velocity measurements using the time-domain methods, most popular due to their simplicity. Successful measurements of phase velocity are usually more accurate than those of group velocity and, also, can be related to Earth structure and anisotropy more unambiguously (Dahlen & Zhou, 2006). Phase-velocity measurements, however, are more complicated than group-velocity ones, even after the unknown initial phase is resolved.

Unlike with the group velocity, converting measured phase or phase travel time to correct phase velocity does not follow a simple relationship of $t = \Delta/c$, where t and c are phase travel time and phase velocity, respectively. Instead, misalignments have been long observed between the monochromatic surface wave and its corresponding Fourier component, $\cos(\omega(t-\Delta/c))$ (Brune et al., 1961; Toksöz & Anderson, 1966; Tromp & Dahlen, 1992; Wang et al., 1993). The misalignments are generally referred to as phase shifts, which must be accounted for during the conversion; otherwise, the resulting phase velocity is biased.

We refer to phase shifts as phase advances or delays (Aki & Richards, 2002; Brune et al., 1961), where a phase advance refers to an event arriving earlier than expected and a phase delay refers to a late arrival. The representation is unambiguous regardless of the sign of frequency and the convention of the Fourier transforms. The value of a phase shift is defined as the amount of deviation of the measured phase from a predicted phase that usually from theoretical approximations. A phase advance, if not corrected, will result in a higher phase velocity, and vice versa. Phase advances and delays corresponds to decreases and increases of the absolute magnitude of the phase in frequency domain, respectively.

A number of types of the phase shifts have been identified. Quantifying and taking them into account is essential for the accuracy of the measurements and for the accuracy of the Earth-structure models computed using the measurements. A phase delay of $\pi/4$ is commonly used in

130 noise cross-correlation studies (e.g., Yao et al., 2006). The phase delay, which is physically
131 generated during interference of surface waves from different noise sources, is referred as (virtual)
132 source phase shift hereafter as it is analogous to the $\pi/4$ phase delay in surface waves generated by
133 earthquakes. The $\pi/4$ is an approximation in the far field (several wavelengths away) of the (virtual)
134 source. The amount of the phase shift changes with distance in the near field. Consequently, most
135 noise cross-correlation studies discard short-distance measurements, e.g., less than 1-3
136 wavelengths (Bensen et al., 2007; Luo et al., 2015; Shapiro et al., 2005). The phase delay turns to
137 a phase advance of $\pi/4$ when using noise cross-correlation functions (NCFs; Kästle et al., 2016)
138 instead of empirical Green's functions (EGFs) that equals the opposite of the first derivative of the
139 NCFs with respect to time.

140 Another type of phase shift is the caustic phase shift. It is generated when surface waves pass
141 a caustic where rays of surface waves cross (e.g., Tromp & Dahlen, 1992; Wang et al., 1993).
142 Surface waves stack constructively at a caustic and change their phase. The caustic phase shift is
143 a $\pi/2$ phase advance in the far field of the caustic. Each passage of a caustic causes a $\pi/2$ phase
144 advance. One example of the caustic phase shift is the polar phase shift (Brune et al., 1961), which
145 occurs when surface waves travel across the antipode of the source and the polar area (the source).
146 The corresponding caustics are exactly at the source and its antipode in a spherically symmetric
147 Earth model and can deviate from the antipode for 10°-20° in a heterogeneous Earth model Earth
148 (Wang et al., 1993). The source phase shift can be regarded as a 'semi-caustic' as well. Its
149 difference from a caustic is that rays converge and diverge at a caustic but only diverge at the
150 source (Brune et al., 1961).

151 In the vicinity (near field) of a caustic or semi-caustic, the phase advance deviates from its
152 far-field value (Kästle et al., 2016; Pollitz, 2001; Schwab & Kausel, 1976; Tromp & Dahlen, 1993;

153 Wielandt, 1980). The exact amount of the phase shift can be either estimated analytically, by
154 adding higher-order terms of Taylor expansions into the analysis (Herrmann, 1973; Wielandt,
155 1980), or computed numerically (Schwab & Kausel, 1976). In this paper, we use near-field phase
156 shifts to refer to the difference between a (semi-)caustic phase shift and its far-field approximation.

157 In the time-domain methods for phase-velocity measurement, approximating monochromatic
158 surface waves by narrowband ones causes additional types of phase shifts due to the interference
159 between neighboring frequencies. The origins of such errors and corresponding solutions have
160 been discussed in the context of group-velocity measurements (Dziewonski & Bloch, 1972;
161 Herrmann, 1973; Levshin et al., 1992; Shapiro & Singh, 1999). The two origins identified are rapid
162 changes in the group-velocity dispersion curve and variations in the amplitude spectra. The
163 proposed solutions for group velocity changes normally involve an iterative procedure that reduces
164 most of the changes in group velocity by subtracting the group velocity measured in the original
165 seismogram (Bensen et al., 2007; Dziewonski & Bloch, 1972; Ritzwoller & Levshin, 1998).
166 Solutions for non-constant amplitude spectra involve replacing the center frequency by an
167 instantaneous frequency (Ritzwoller & Levshin, 1998) or a centroid frequency (Shapiro & Singh,
168 1999).

169 The narrow-band approximation also has an effect on phase-velocity measurements. To our
170 knowledge, however, there are no systematic studies on the associated phase shifts and their effects
171 on the measurements and the resulting Earth models, especially in the context of noise cross-
172 correlations. Herrmann (1973) showed an additional phase term in the mathematical representation
173 of Gaussian filtered surface waves, but he did not discuss its further implication.

174 The purpose of this paper is to present a systematic study of—and practical ways to correct
175 for—the phase shift caused by approximating monochromatic surface waves by narrow-band

surface waves. We refer to the phase shift as the finite-frequency phase shift, as it originates from a replacement of an infinitesimally narrow frequency band by a finite-width band. We first derive an explicit expression of the phase shift, under certain assumptions, and then present a numerical method to accurately evaluate the phase shift. We also demonstrate the effect of the finite-frequency phase shift on the phase velocity measurements and offer recipes for the correction of the phase shift in order to obtain accurate phase-velocity measurements. The results apply to measurements with time-domain methods on surface waves from earthquakes, active sources and ambient seismic noise.

2 Finite-frequency phase shift

Surface waves at different frequencies travel at different speeds. To measure phase velocities at different frequencies, a comb of narrow-bandpass filters is often used to isolate individual frequencies, such as in the multiple filter technique (Dziewonski et al., 1969). The filtered surface wave resembles a cosine function with a period of $1/f_c$, where f_c is the center frequency of the filters (Figure 1a). Assuming the narrowband surface waves share the same peaks with the monochromatic surface waves, the arrival time of the peaks can be written explicitly,

$$t_n = \frac{\Delta}{c} + \frac{1}{8f_c} + \frac{n}{f_c} + \frac{\phi_s}{\omega_c}, \quad n = 0, \pm 1, \pm 2, \dots, \tag{1}$$

where Δ is the distance, c the phase velocity at the frequency f_c, $\omega_c = 2\pi f_c$ the angular frequency, ϕ_s the initial phase of the source (Dahlen & Tromp, 1998; Yao et al., 2006). The $1/(8f_c)$ is the manifestation of the $\pi/4$ phase delay caused by the source term. We refer to n as the order of peaks in the narrowband surface waves, or 'ridges' in the frequency-time representation (Figure 1b). The 0th ridge is often referred as the 'correct' ridge (e.g., Wang et al., 2017; Yao et al., 2006), though

197 other ridges can also generate correct phase velocity measurements if the time shift n/f_c is corrected
198 (Bonadio et al., 2018; T. Meier et al., 2004; Soomro et al., 2016; Xu et al. 2021).

199 The finite-frequency phase shift, $\delta\phi$, corresponds to the time offset δt (= $\delta\phi/2\pi f_c$) between the
200 peaks of the narrowband and monochromatic surface waves (Figure 1c), giving a more accurate
201 prediction of the arrival time of the peaks,

202 $$t_n = \frac{\Delta}{c} + \frac{1}{8f_c} + \frac{n}{f_c} + \frac{\phi_s}{\omega} + \delta t, \quad n = 0, \pm 1, \pm 2, \ldots . \tag{2}$$

203 Unlike the 'systematic error' due to the variations in amplitude spectra, discussed by Shapiro and
204 Singh (1999), the phase shift is non-zero even for constant amplitude spectra. It needs to be
205 corrected along with the $\pi/4$ phase delay to get an accurate measurement of phase velocities,

206 $$c = \frac{\Delta}{t - 1/8f_c - n/f_c - \phi_s/\omega_c - \delta t}, \tag{3}$$

207 or

208 $$c = \frac{\omega_c \Delta}{\omega_c t - \pi/4 - 2n\pi - \phi_s - \delta\phi}. \tag{4}$$

209 Figure 2 illustrates the origin of the finite-frequency phase shift. Monochromatic surface
210 waves are generated at three equal-spaced frequencies, 0.99, 1.00 and 1.01 Hz. Superposition of
211 the three produces a narrow-band surface wave (Figure 2b, c). The three monochromatic surface
212 waves have the same amplitude, so as to avoid the influence of the spectral amplitude variation.
213 When the phase velocity dispersion curve is linear, the peak in the narrow-band surface wave
214 arrives at the same time as the peak of the center-frequency (1 Hz) surface wave. By contrast,
215 when the dispersion curve is not linear, the two peaks have a slight misalignment. The

misalignment is the finite-frequency phase shift. If not accounted for, the misalignment will result in a biased phase velocity measurement.

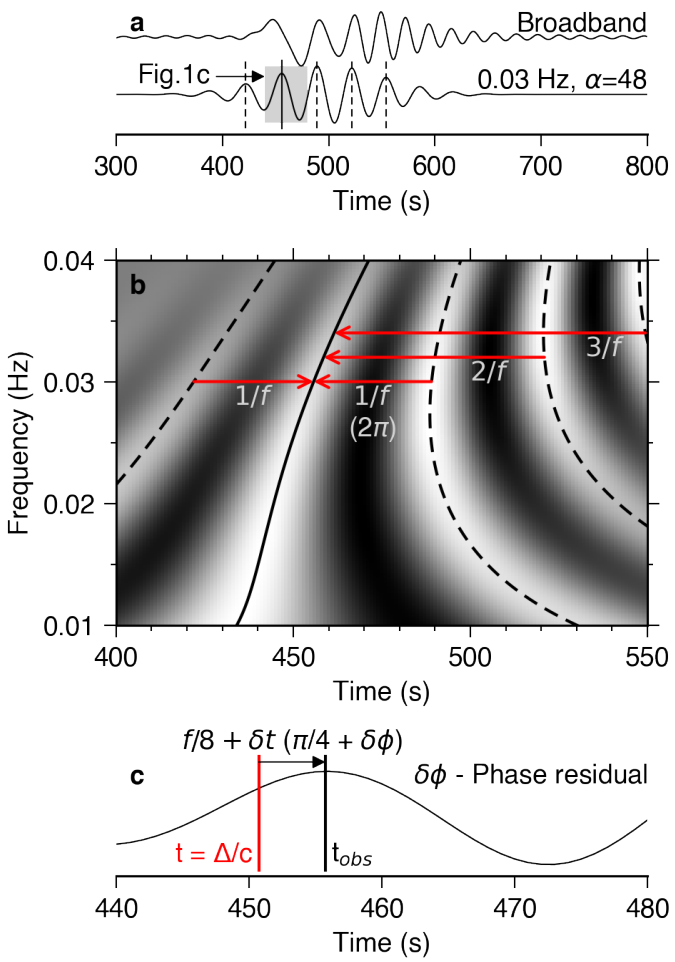

Figure 1 Time-domain phase velocity measurement and the finite-frequency phase shift. (a) Broadband and narrow-bandpass-filtered surface waves. The broadband surface wave is a synthetic seismogram generated using the velocity model ak135 (Kennett et al., 1995). For the narrow-band surface wave, a Gaussian filter with the center frequency of 0.03 Hz and $\alpha = 48$ is used. The arrival times of the peaks are marked by vertical lines, with the peak corresponding to the correct phase travel time marked by a solid line and other peaks by dashed lines. (b) Frequency-time representation of the broadband surface wave.

Each row of the image corresponds to a narrow-band filtered surface wave. Connected peaks form ridges, with the 'correct' ridge marked by a solid line and other ridge by dashed lines. The separation between these ridges are n/f, or $2n\pi$ in phase. (c) The finite-frequency phase shift. The measured phase travel time is $f/8+\delta t$ s later than the predicted phase travel time of Δ/c, equivalent to a $\pi/4+\delta\phi$ phase delay, where $\delta\phi$ is the finite-frequency phase shift.

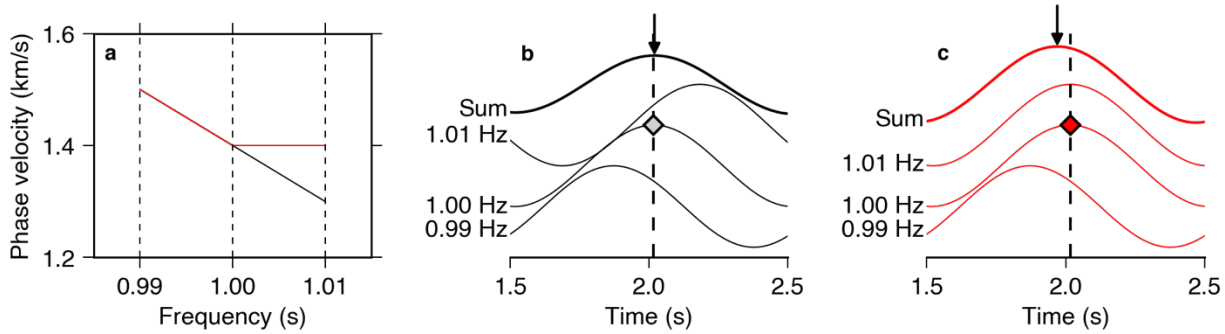

Figure 2 Finite-frequency phase shift caused by using a bundle of frequencies to estimate the centre frequency. (a) Phase velocity curves used in the example. The black line denotes the curve that is linear, whereas the red line denotes a curve with a curvature (the kink at 1 Hz). (b) Monochromatic components at 0.99, 1.00 and 1.01 Hz and their superposition. The linear curve is used. The diamond and the dashed line mark the arrival time of the peak of the 1-Hz component. The arrow points to the arrival time of the peak of the superposition. (c) Same as b but using the curve with the kink.

3 Theoretical derivation

We can derive an explicit expression for the finite-frequency phase shift assuming the far field approximation and narrow frequency bands. By far field, we mean large $|\omega|\Delta/c = 2\pi\Delta/\lambda$, that is, a large number of wavelengths fitting between the source and station, or between two stations in the case of noise interferometry and two-station methods. Starting from the spectrum of surface waves, we integrate the spectrum over frequency in order to obtain the seismogram of surface waves, to which we refer as broadband surface waves. Then, we apply Gaussian filters to obtain the explicit

expression for the narrow-band surface waves, from which, finally, we obtain the explicit expression for the finite-frequency phase shift.

3.1 Stationary phase approximation

The stationary phase approximation method is used repeatedly in the following derivation in order to approximate integrals. We briefly summarize the points that are relevant to our derivation. For more details, we refer the reader to Aki and Richards (2002). The method is used to estimate the integral of the form

$$\int_a^b F(\omega)\exp\big(f(\omega)\big)d\omega, \tag{5}$$

where $F(\omega)$ and $f(\omega)$ are real functions and ω is a dummy variable that does not necessarily mean frequency. Both a and b can be infinity. This type of integral is dominated by several discrete points where $f'(\omega) = 0$. They are termed stationary phase points or saddle points (after the shape of the integrand surface near these points in the complex domain of ω. If the $|f''(\omega)|$ values at the saddle points are sufficiently large, the integral can be estimated as a summation of the contribution of the saddle points,

$$\sum_{\omega_0 \in saddle\ points} F(\omega_0)\exp\big(f(\omega_0)\big)\sqrt{\frac{2\pi}{|f''(\omega_0)|}} \times \begin{cases} \exp\left(i\dfrac{\pi-\phi}{2}\right), & \phi \in (0,\pi] \\ \exp\left(i\dfrac{-\pi-\phi}{2}\right), & \phi \in (-\pi,0) \end{cases}, \tag{6}$$

where ω_0 are saddle points within the interval $[a, b]$ and $\phi = \arg f''(\omega_0)$. When a saddle point is at the end of the interval, its contribution should be halved.

3.2 Broadband time-domain waveforms

Surface waves can be written as a superposition of monochromatic surface waves,

$$x(t) = \frac{1}{\pi}\Re\int_0^{+\infty} A(\omega)\exp\left(-i\frac{\omega\Delta}{c(\omega)} + i\varphi(\Delta)\right)\exp(i\omega t)\,d\omega\,, \tag{7}$$

where $\Re$ is the real part operator that arises from the reduction of the interval (-∞, +∞) to [0, +∞) using the Hermitian symmetry of the spectrum, $A(\omega)$ is the amplitude spectrum, and $\varphi(\Delta)$ represents the overall phase shift regarding propagation of monochromatic surface waves, comprising the initial phase from the source mechanism, the source phase shift and the caustic phase shift when passing a polar or antipodal region. The Fourier transform we used is

$$F(\omega) = \int_{-\infty}^{+\infty} f(t)\exp(-i\omega t)\,dt\,,$$

$$f(t) = \frac{1}{2\pi}\int_{-\infty}^{+\infty} F(\omega)\exp(i\omega t)\,d\omega\,, \tag{8}$$

although the conclusion is independent of the convention of Fourier transform. For any given distance, equation 7 can be evaluated using the stationary phase approximation,

$$x(t) \approx \sqrt{\frac{2}{\pi\Delta|k''(\omega_0)|}} \times \begin{cases} \cos\left(\omega_0 t - k(\omega_0)\Delta + \varphi - \frac{\pi}{4}\right), & k''(\omega_0) > 0 \\ \cos\left(\omega_0 t - k(\omega_0)\Delta + \varphi + \frac{\pi}{4}\right), & k''(\omega_0) < 0 \end{cases}, \tag{9}$$

where $k(\omega) = \omega/c(\omega)$ is the wavenumber and $k'(\omega_0) = t/\Delta$. It shows that the instantaneous phase of broadband surface waves deviates from its corresponding monochromatic component by $\pm\pi/4$, depending on the sign of $k''(\omega_0)$. $k''(\omega_0)$ is positive when $\mathrm{d}c_g/\mathrm{d}T > 0$, where $c_g = \mathrm{d}\omega/\mathrm{d}k$ is group velocity and $T = 2\pi/\omega$ is period. The corresponding frequency for each time t can be found by solving $k'(\omega_0) = t/\Delta$.

3.3 Narrowband time-domain waveforms

3.3.1 Far-field approximation

Bandpass filtering can change the instantaneous phase of surface waves. Applying a Gaussian filter to the broadband surface wave (equation 7), we have

$$x(t) = \frac{1}{\pi}\Re\int_0^{+\infty} A(\omega)\exp\left(-i\frac{\omega\Delta}{c(\omega)} + i\varphi(\Delta)\right)\exp\left(-\alpha\frac{(\omega-\omega_c)^2}{\omega_c^2}\right)\exp(i\omega t)\,d\omega\,, \qquad (10)$$

where ω_c is the center frequency of the filter and α (> 0) is a parameter that controls the width of the filter. Using the stationary phase approximation, we can obtain the explicit expression for the time-domain waveform of the filtered surface wave,

$$x(t) \approx \sqrt{\frac{2}{\pi\left|ik''\Delta + \frac{2\alpha}{\omega_c^2}\right|}}A(\omega_0)\exp\left(-\alpha\frac{(\omega_0-\omega_c)^2}{\omega_c^2}\right) \times \begin{cases}\cos\left(\omega_0 t - k\Delta + \varphi(\Delta) + \dfrac{-\pi-\beta}{2}\right), & k''(\omega_0) > 0\\ \cos\left(\omega_0 t - k\Delta + \varphi(\Delta) + \dfrac{\pi-\beta}{2}\right), & k''(\omega_0) < 0\end{cases}, \qquad (11)$$

where the stationary phase point ω_0 is determined by

$$-ik'(\omega_0)\Delta + it - 2\alpha\frac{\omega_0-\omega_c}{\omega_c^2} = 0, \qquad (12)$$

and

$$\beta = \arg f''(\omega) = \arg\left(-\frac{2\alpha}{\omega_c^2} - ik''(\omega_0)\Delta\right). \qquad (13)$$

When using a wide-band Gaussian filter ($\alpha\to 0$), β in equation 11 approaches $-\pi/2$ for $k''(\omega_0) > 0$ and $\pi/2$ for $k''(\omega_0) < 0$. Thus, equation 11 degenerates to its broadband counterpart, equation 9. When using a narrow-band filter ($\alpha\to\infty$), $\beta\to-\pi$ ($k''(\omega_0) > 0$) and π ($k''(\omega_0) < 0$), the cosine term

296 in equation 11 in both cases become $\cos(\omega_0 t - k\Delta + \varphi(\Delta))$, which has the same phase as the
297 monochromatic surface waves in equation 7. This is why narrow-bandpass filtered surface waves
298 can be used to measure phase velocity at the center frequencies of the filters. However, α cannot
299 be ∞ when making real measurements. It is crucial to know how much is the error for using a finite
300 α. As the saddle points move away from the real axis into the complex domain for $0 < \alpha < \infty$, it is
301 not trivial to evaluate the phase shift using the stationary phase approximation, so we turn to
302 another approximation under the narrow-band assumption.

303 3.3.2 Far-field and narrow-band approximation

304 To obtain an explicit expression for the finite-frequency phase shift, we re-evaluate the
305 integral in equation 10 using Taylor expansions at the center frequency ω_c. In additional to the far-
306 field approximation, we limit ourselves to narrow-band filters. In this case, let

307 $$F(\omega) = \frac{A(\omega)}{\pi},$$

308 $$f(\omega) = \omega t - k\Delta + \varphi(\Delta), \tag{14}$$

309 we can expand $F(\omega)$ and $\exp(if(\omega))$ at ω_c,

310 $$\begin{aligned} F(\omega) &\approx F(\omega_c) + F'(\omega_c)(\omega - \omega_c) + \frac{1}{2}F''(\omega_c)(\omega - \omega_c)^2 \\ \exp\big(if(\omega)\big) &\approx \exp\big(if(\omega_c)\big)\left[1 + if'(\omega_c)(\omega - \omega_c) + \frac{1}{2}(if''(\omega_c) - f'^2(\omega_c))(\omega - \omega_c)^2\right] \end{aligned}. \tag{15}$$

311 Substituting equation 15 into equation 10, the integral can be organized as a series of integrals ∫
312 $(\omega-\omega_c)^n \exp(-\alpha(\omega-\omega_c)^2)d\omega$, which can be evaluated analytically. Summing the results yields the
313 expression for the time-domain waveform of narrowband surface waves,

314 $$x(t) \approx \frac{A(\omega)B}{\pi}\omega_c\sqrt{\frac{\pi}{\alpha}}\cos\big(i(\omega t - k\Delta + \varphi(\Delta) - \delta\phi)\big), \tag{16}$$

where B and $\delta\phi$ are the amplitude and phase, respectively, of a complex number given by

$$B\exp(i\delta\phi) = F(\omega_c) + \frac{\omega_c^2}{2\alpha}\left[-\frac{1}{2}F(\omega_c)f'^2(\omega_c) + \frac{1}{2}F''(\omega_c)\right] - i\frac{\omega_c^2}{2\alpha}\left[\frac{1}{2}F(\omega_c)f''(\omega_c) + F'(\omega_c)f'(\omega_c)\right]. \quad (17)$$

The $\delta\phi$ is the finite-frequency phase shift we are looking for. We intentionally use $-\delta\phi$ instead of $\delta\phi$ in equation 16, so that $\delta\phi > 0$ corresponds to phase delay and $\delta\phi < 0$ corresponds to phase advance.

Assuming a constant amplitude spectrum, $F'(\omega_c)$ and $F''(\omega_c)$ are zero. Therefore, we can evaluate the finite-frequency phase shift as

$$\delta\phi = \arg\left\{\frac{4\alpha}{\omega_c^2} - (t - k'(\omega_c)\Delta)^2 + ik''(\omega_c)\Delta\right\}. \quad (18)$$

For narrow-band filters when α is sufficiently large, the first term dominates the real part. We can therefore simplify the mathematical representation of $\delta\phi$ to

$$\delta\phi = \arctan\frac{k''(\omega_c)\Delta}{4\alpha/\omega_c^2} \approx \frac{\omega_c^2 k''(\omega_c)\Delta}{4\alpha} \quad (19)$$

The formula in equation 19 reveals four factors that affect the finite-frequency phase shift, namely, (1) the center frequency of the Gaussian filter ω_c, (2) the second derivative of the wavenumber with respect to frequency $k''(\omega_c)$, (3) the epicentral distance Δ and (4) the width of the Gaussian filter α. Since ω_c, Δ and α are all positive, the sign of the phase shift is solely determined by $k''(\omega_c)$. Physically, $k''(\omega_c) > 0$ means a positive curvature (with respect to frequency) in the phase dispersion curve or a positive slope (with respect to period) in the group dispersion curve.

3.4 Finite-frequency phase shift in noise cross-correlation functions

Here we show that the finite-frequency phase shift in the surface waves in the noise cross-correlation functions (NCFs) shares exactly the same formula with ballistic surface waves. First,

we compute the spectrum of NCFs by summing the cross-correlation of incoming plane waves over all the azimuths. Assuming that we have two stations, station A and station B, separated by the distance Δ, and an incoming plane wave that arrives at the angle θ (measured counter-clockwise from the east) (Figure 3), the cross-correlation spectrum of the plane wave at the station A with one at station B is $\exp(i\omega\Delta\cos\theta/c)$, where ω is the angular frequency and c is the phase velocity at this frequency. Assuming a perfect illumination, when the amplitude of the incoming plane waves is constant over azimuth, the spectrum of the noise cross-correlation can be written as

$$C(\omega) = \frac{1}{2\pi}\int_{-\pi}^{\pi} \exp\left(i\omega\frac{\Delta\cos\theta}{c(\omega)}\right) \mathrm{d}\theta = J_0\left(\frac{\omega\Delta}{c(\omega)}\right), \tag{20}$$

where J_0(x) is the zeroth-order of Bessel functions of the first kind. Evaluating the integral using the stationary phase approximation yields the far-field approximation of the spectrum of the noise cross-correlation,

$$C(\omega) \approx \sqrt{\frac{2}{\pi\frac{|\omega|\Delta}{c(\omega)}}}\cos\left(\frac{|\omega|\Delta}{c(\omega)} - \frac{\pi}{4}\right). \tag{21}$$

where far field implies a large $\omega\Delta/c = 2\pi\Delta/\lambda$ and λ is the wavelength. Alternatively, the approximation can be obtained using asymptotic forms of Bessel functions (Gradshteyn & Ryzhik, 2014). The contributions of the causal branch and the acausal branch can also be separated in the far-field approximation (Table 1).

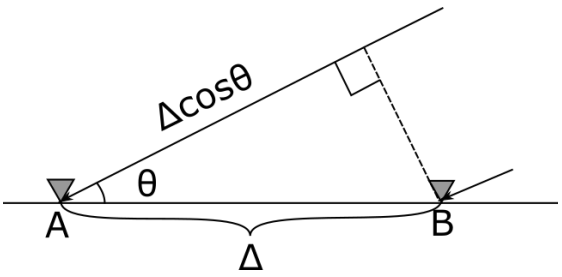

Figure 3 Incoming plane wave at a pair of stations. The plane wave arrives at the stations at an angle θ. The distance between stations A and B is Δ. The plane wave needs to travel farther by $\Delta\cos\theta$ to reach station A compared to station B. The corresponding time delay is $\Delta\cos\theta/c$ and phase delay is $\omega\Delta\cos\theta/c$.

Table 1 Spectra of the causal and acausal branches of the noise cross-correlation under the far-field approximation. The common factor $\sqrt{2c(\omega)/\pi|\omega|\Delta}$ is omitted. The expressions correspond to the convention of Fourier transforms indicated by equation 8. Using other conventions will result in changes of signs or an additional constant factor.

Branch	$\boldsymbol{\omega > 0}$	$\boldsymbol{\omega < 0}$
Causal	$\exp\left(-i\left(\frac{\omega\Delta}{c(\omega)}-\frac{\pi}{4}\right)\right)$	$\exp\left(-i\left(\frac{\omega\Delta}{c(\omega)}+\frac{\pi}{4}\right)\right)$
Acausal	$\exp\left(i\left(\frac{\omega\Delta}{c(\omega)}-\frac{\pi}{4}\right)\right)$	$\exp\left(i\left(\frac{\omega\Delta}{c(\omega)}+\frac{\pi}{4}\right)\right)$

Applying inverse Fourier transform to the far-field approximation of the spectrum of the causal branch (Table 1) yields the expression of broadband surface waves in the causal branch of NCFs,

$$
\begin{aligned}
C_+(t) &\approx \frac{1}{2\pi^2}\Re\int_0^\infty \sqrt{\frac{2\pi}{k\Delta}}\exp(i\omega t - ik\Delta)\exp\left(i\frac{\pi}{4}\right)d\omega \\
&\approx \frac{1}{\pi\Delta}\frac{1}{\sqrt{|k(\omega_0)||k''(\omega_0)|}}\times\begin{cases}\cos(\omega_0 t - k(\omega_0)\Delta), & k''(\omega_0) > 0\\ \cos\left(\omega_0 t - k(\omega_0)\Delta + \frac{\pi}{2}\right), & k''(\omega_0) < 0\end{cases}
\end{aligned}
\tag{22}
$$

where $k'(\omega_0) = t/\Delta$. We can also obtain the expression for the surface waves in the acausal branch,

$$C_{-}(t) \approx \frac{1}{\pi\Delta}\frac{1}{\sqrt{|k(\omega_0)||k''(\omega_0)|}} \times \begin{cases} \cos(\omega_0 t + k(\omega_0)\Delta), & k''(\omega_0) > 0 \\ \cos\left(\omega_0 t + k(\omega_0)\Delta - \frac{\pi}{2}\right), & k''(\omega_0) < 0 \end{cases} \quad (23)$$

where $k'(\omega_0) = -t/\Delta$ ($t < 0$). The two branches form an even function of t.

Unlike the ballistic surface waves, surface waves in NCFs have a known $\pi/4$ advance instead of an unknown phase shift of $\phi(\Delta)$. However, the $\pi/4$ phase advance can be cancelled out by the $\pi/4$ phase delay that arises in the frequency integration when $k''(\omega_0) > 0$, making the instantaneous phase of the surface wave at a certain time t is in-phase (no phase shift) with the corresponding monochromatic surface wave $\cos(\omega_0 t - \omega_0\Delta/c(\omega_0))$. To illustrate the phenomenon, we generate a broadband surface-wave synthetic using the exact spectrum in equation 20 and ak135 (Kennett et al., 1995) and then compare it with the monochromatic surface wave (Figure 4). The alignment is easier to examine at the peaks, so we chose the frequency 0.0355 Hz that is the saddle point corresponding to the peak at t = 901.27 s. A good consistency is observed between the monochromatic and broadband surface waves at 901.27 s, confirming their alignment in terms of phase. Furthermore, the instantaneous frequency at 901.27 s is also 0.0355 Hz, which can be verified by computing the first derivative of the instantaneous phase $\phi(t) = \omega_0 t - k(\omega_0)\Delta$, which is

$$\omega(t) = \frac{\partial\phi(t)}{\partial t} = \omega_0 + \frac{\partial\omega_0}{\partial t}(t - k'(\omega_0)\Delta) = \omega_0(t) \quad (24)$$

in the causal branch. The second term is zero because the saddle point ω_0 follows the relationship $k'(\omega_0) = t/\Delta$.

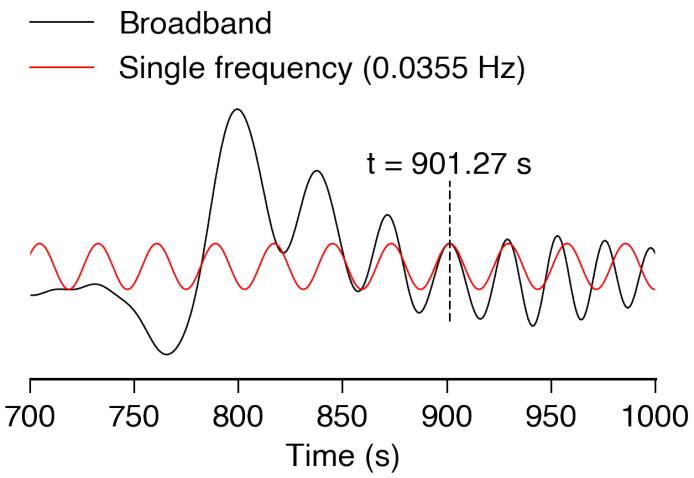

383

384 **Figure 4**. Broadband and monochromatic surface waves. The broadband surface wave synthetic is
385 computed using a trapezoid integration from 2 to 50 mHz, with an interval of 0.01 mHz. There is no
386 misalignment between the peak at t = 901.27 s and its corresponding single frequency component, as the
387 phase delay of π/4 that arises from the frequency integration is cancelled by the phase advance of π/4 that
388 arises from the integration over azimuth.

389

390 The narrowband time-domain waveforms of NCFs can be computed using the same approach
391 as in Section 3.3,

392
$$C(t) \approx \frac{1}{2\pi^2}\Re\int_0^\infty \sqrt{\frac{2\pi}{k\Delta}}\exp(i\omega t - ik\Delta)\exp\left(i\frac{\pi}{4}\right)\exp\left(-\alpha\frac{(\omega_0-\omega_c)^2}{\omega_c^2}\right)d\omega$$
$$\approx \frac{B}{2\pi^2}\omega_c\sqrt{\frac{\pi}{\alpha}}\Re\left\{\exp\left(i\left(\omega t - k\Delta + \frac{\pi}{4} - \delta\phi\right)\right)\right\}, \quad (25)$$

393 where B and $\delta\phi$ share exactly the same definition as ballistic surface waves, with a slightly different
394 definition of $F(\omega)$ and $f(\omega)$,

395
$$F(\omega) = \frac{1}{2\pi^2}\sqrt{\frac{2\pi}{k\Delta}},$$

$$f(\omega) = \omega t - k\Delta + \frac{\pi}{4}. \quad (26)$$

Despite that difference in $F(\omega)$ and $f(\omega)$, surface waves from noise interferometry share the identical formula for the finite-frequency phase shift with surface waves from earthquakes and active sources,

$$\delta\phi \approx \frac{\omega_c^2 k''(\omega_c)\Delta}{4\alpha}. \quad (27)$$

3.5 Finite-frequency phase shift in two-station methods

The two-station method is commonly used to measure phase velocities when the initial phase of the source is unknown (e.g., Brilliant & Ewing, 1954; T. Meier et al., 2004; Kolínský et al., 2019). It avoids the initial phase by measuring the travel time difference between two stations that are in line with the source. The difference can be captured by cross-correlating the surface waves on the two stations, whose spectrum has the following form,

$$C(\omega) = \exp\left(-i\frac{\omega\Delta}{c(\omega)}\right). \quad (28)$$

The narrowband surface waves can be obtained following the same procedure as in the ballistic and noise cross-correlation cases,

$$C(t) \approx \frac{1}{\pi}\Re\int_0^\infty \exp(i\omega t - ik\Delta)\exp\left(-\alpha\frac{(\omega_0-\omega_c)^2}{\omega_c^2}\right)d\omega \approx \frac{B}{\pi}\omega_c\sqrt{\frac{\pi}{\alpha}}\Re\{\exp(i(\omega t - k\Delta - \delta\phi))\}. \quad (29)$$

Again, the finite-frequency phase shift is,

$$\delta\phi \approx \frac{\omega_c^2 k''(\omega_c)\Delta}{4\alpha}. \quad (30)$$

4 Numerical computation of the finite-frequency phase shift

To evaluate the finite-frequency phase shift accurately without the far-field and narrow-band assumptions, we now compute it numerically. The results can be used to correct the errors in phase-velocity measurements caused by this specific phase shift.

We compute the phase shift by comparing the measured phase travel times, obtained from surface-wave synthetics, to their far-field prediction, given by $t_0 = \Delta/c(f_c) - 1/(8f_c)$. The computation only needs a phase dispersion curve, $c = c(f)$. As for the "measured" phase travel time, we first generate a synthetic surface wave by superposing monochromatic surface waves. Here, we use the exact expression of the causal branch of monochromatic noise cross-correlation functions,

$$\sum_{i=0}^{N-1} w_i \Re\left[\left(H_0^{(2)}\left(\frac{\omega_i \Delta}{c(f_i)}\right)\right)\exp(i\omega_i t)\right]\mathrm{d}f, \qquad f_i = f_0 + i\mathrm{d}f, \tag{31}$$

where $H_0^{(2)}(x)$ is the zeroth-order Hankel functions of the second kind, $\omega_i = 2\pi f_i$, and w_i is the weighting coefficient determined by the integration method used. The results apply to ballistic surface waves as well. For two-station methods, one should replace the Hankel functions by cosine functions, but they share the same far-field patterns. We use the trapezoidal integration, with w_i = 0.5 when $i = 0$, N-1 and $w_i = 1$ when $i = 1, \ldots, N$-2. Next, we measure the phase travel time using the method of Xu et al. (2021), who used a frequency-dependent $\alpha = 2\pi f\gamma^2$, with γ being an empirical parameter (Soomro et al., 2016). Finally, we compute the difference δt between the measured and predicted phase travel times and multiply it by $2\pi f_i$ to get the finite-frequency phase shift $\delta\phi$. The process should be repeated for each distance. For dense arrays, we can accelerate the computation by interpolating a phase shift table pre-computed at a set of distance. The phase

velocity measurement method should be the same as the one used to obtain the real measurements so as to avoid introducing errors due to the difference in the measurement methods.

In order to correct the finite-frequency phase shift in a real phase-velocity dataset, we need a phase dispersion curve. A good start is the average dispersion curve or a reference model inverted from the dataset. We recommend the reference-model approach as the dispersion curve it generates is free of unphysical bumps. Once the phase shift $\delta\phi$ is computed, one can correct the phase velocity by

$$\frac{1}{c} = \frac{1}{\tilde{c}} - \frac{\delta\phi}{\omega\Delta} \tag{32}$$

where $\tilde{c}$ and c is the phase velocity before and after the correction.

Figure 5 illustrates the computation of the finite-frequency phase shift for a station pair separated by 250 km. We used a phase dispersion curve calculated using ak135 to generate the broadband surface-wave synthetic (Herrmann, 2013; Figure 5a). We integrated from 2 to 50 mHz with an interval of 0.01 mHz. The phase travel time is measured on the narrow-band-passed waveforms. The resulting phase shift is mostly positive (phase delay; Figures 5b,e), except for low frequencies (Figures 5c,e). We found that this low-frequency anomaly is related to the near-field phase shift, which we discuss further in Section 5.1. The phase shift causes noticeable perturbations in the corresponding "measured" phase velocity curve (up to 0.02 km/s; Figures 5f,g).

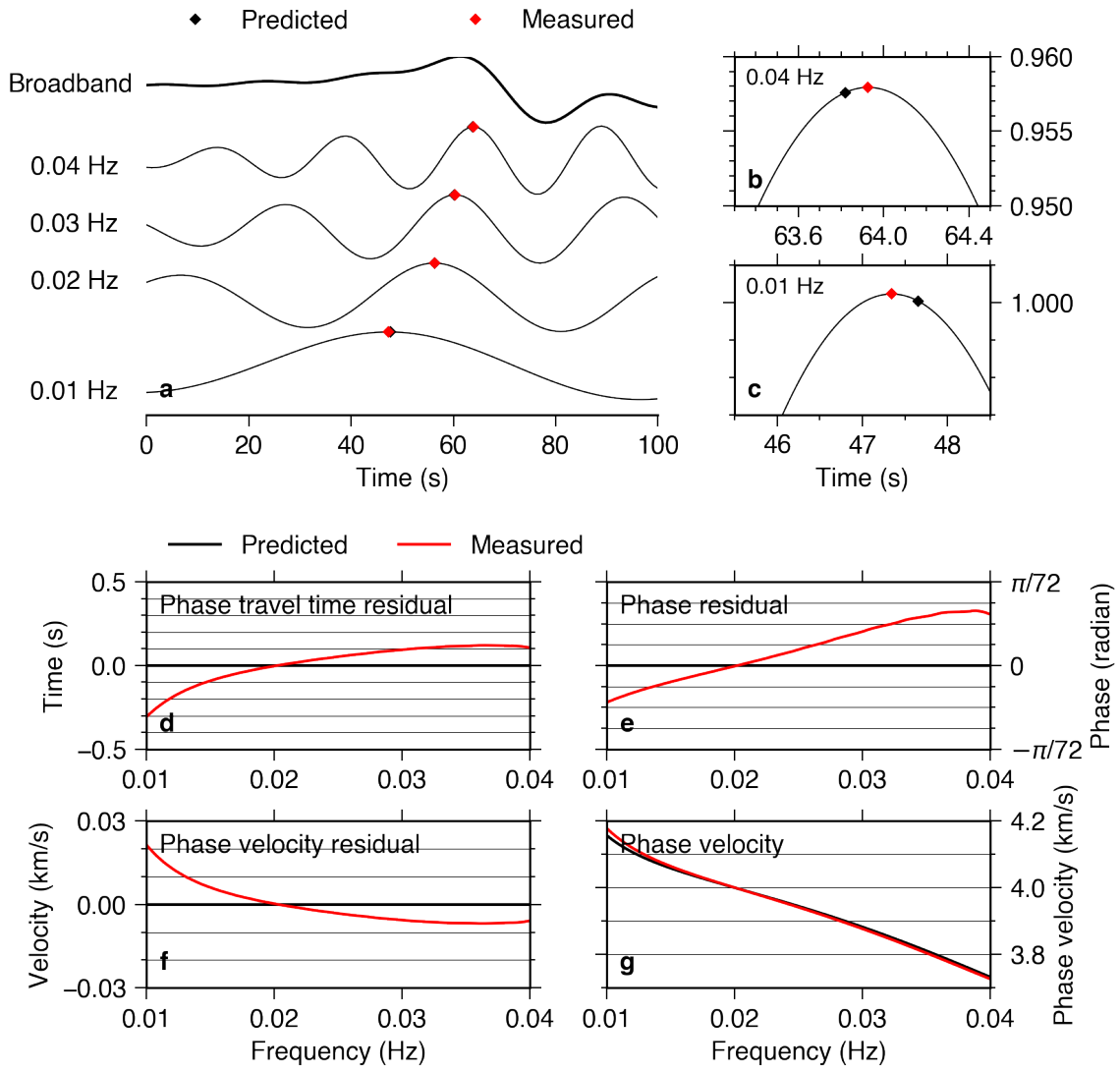

Figure 5 Numerical computation of the finite-frequency phase shift. (a) Broadband synthetic and narrow-band filtered synthetics. We use $\gamma = 16$ to determine the width of the Gaussian filters, the same as Soomro et al. (2016) used for station pairs with similar distance ranges. Red and black diamonds denote the measured and predicted phase travel time, respectively. (b) Zoom-in around the measured phase travel time of the filtered synthetic around 0.04 Hz. (c) Same as b, but for 0.01 Hz. (d) Phase travel time residual, the difference between the measured (red) and predicted (black) phase travel time. (e) Corresponding phase residual. (f) Corresponding phase velocity residual. (g) Measured and predicted phase velocity dispersion curve.

461 ### 4.1 High-frequency example (1-25 Hz)

462 We now compute the phase shift in a high-frequency scenario, relevant for the surface wave
463 imaging of the shallow crust. We use this to demonstrate how to use the numerical method and to
464 illustrate the factors that control the finite-frequency phase shift.

465 We use a model of the Dublin Basin, simplified from one obtained previously using receiver
466 functions (Licciardi & Piana Agostinetti, 2017). The model has 4 layers and a half space below
467 them (Figure 6a; Table 2). The P-wave velocity and density are converted from the S velocity
468 using the formulas in Brocher (2005). After computing the Rayleigh-wave phase-velocity
469 dispersion curve, we evaluate the phase shift for interstation distances from 0.5 to 4 km, at a 0.1
470 km step (Figure 6b). For each distance, we compute the synthetics using equation 31 and a
471 frequency range of 0.1-30 Hz, with an interval of 0.01 Hz (Figure 6c). We select 51 frequency
472 points logarithmically distributed between 0.1 and 30 Hz as the center frequencies of the Gaussian
473 filters. Figure 6d shows an example of the finite-frequency phase shift measured for the Gaussian
474 filter with a center frequency of 5 Hz, which is 0.142 radians.

475 We use $\gamma = 1$ to compute the finite-frequency phase shift over the distance range of 0.5-4 km
476 and the frequency range of 1-25 Hz (Figure 7; A slightly smaller $\gamma = 0.5$ is used, for clarity, in
477 Figure 6c). The amplitude of the phase shift ranges from -0.015 to $0.026\,\pi$, much smaller than the
478 $\pi/4$ phase shift caused by the source. The prominent features are the two high-amplitude anomalies
479 around 5 and 1.4 Hz. These are the frequencies of the two peaks in the second derivative of the
480 wavenumber, $k''(\omega)$, which confirms the effect predicted by the equation 27. The effect of the
481 distance is clear as well. The amplitudes of the two anomalies decrease with decreasing distance,
482 from $0.026\,\pi$ at 4 km to $0.0019\,\pi$ at 0.6 km. Additionally, the phase shift increases linearly with

483 frequency due to a combined effect of ω^2 and the frequency-dependent α. It makes the 5-Hz
484 anomaly stronger than the 1.4-Hz anomaly despite a smaller $k''(\omega)$ at 5 Hz.

485 The corresponding phase-velocity perturbation (−0.79% to 2.3%) shows a pattern from that
486 for the phase shift (Figure 8). Firstly, the sign of the phase-velocity perturbation is opposite to the
487 phase shift. That is because a positive phase shift causes a delay in travel time, translating to a
488 lower phase velocity. Secondly, the change of amplitude with distance disappears and the change
489 with frequency is proportional to $k''(\omega)$. The reason is that the effects of distance and frequency
490 cancel out when the phase shift is converted to phase velocity (equation 3). Therefore, the
491 amplitude variation in the phase shift table only depends on $k''(\omega)$. The frequency dependence is
492 cancelled when α changes linearly with frequency. Using a constant α, instead, results the velocity
493 perturbation depends linearly on frequency. The positive anomaly observed in the lower-right
494 corner of Figure 8 corresponds to low frequency and short distance or, equivalently, the near field
495 (small Δ/λ). The distinctive feature is a result of the near-field effects rather than the finite-
496 frequency phase shift, as we discuss further in Section 5.1.

497 The finite-frequency phase shift is larger if a smaller γ is used, when the width of filter widens
498 to include more frequencies (Figure 9). The phase shifts range from $-\pi/128$ to $7\pi/128$ for $\gamma = 0.5$,
499 with a group of filters centered at 0.05, 0.1, 0.2 and 0.5 s. The phase shifts decrease when γ
500 increases and converge to a small (non-zero) value determined by the near-field effects. However,
501 using a large γ in real-data applications may reduce the signal-to-noise ratio in the filtered surface
502 waves, hence increasing errors in phase velocity measurements. Therefore, the problem of the
503 finite-frequency phase shift cannot be solved by simply adopting a large γ.

504

505 **Table 2**. Velocity model of the Dublin Basin simplified after Licciardi & Piana Agostinetti (2017).

Layer No.	Layer thickness (km)	Vp (km/s)	Vs (km/s)	Density (g/cm^3)
1	0.15	4.17	2.44	2.42
2	0.5	4.85	2.88	2.51
3	1.35	5.49	3.25	2.62
4	8.0	5.96	3.5	2.71
5	∞	6.34	3.7	2.79

506

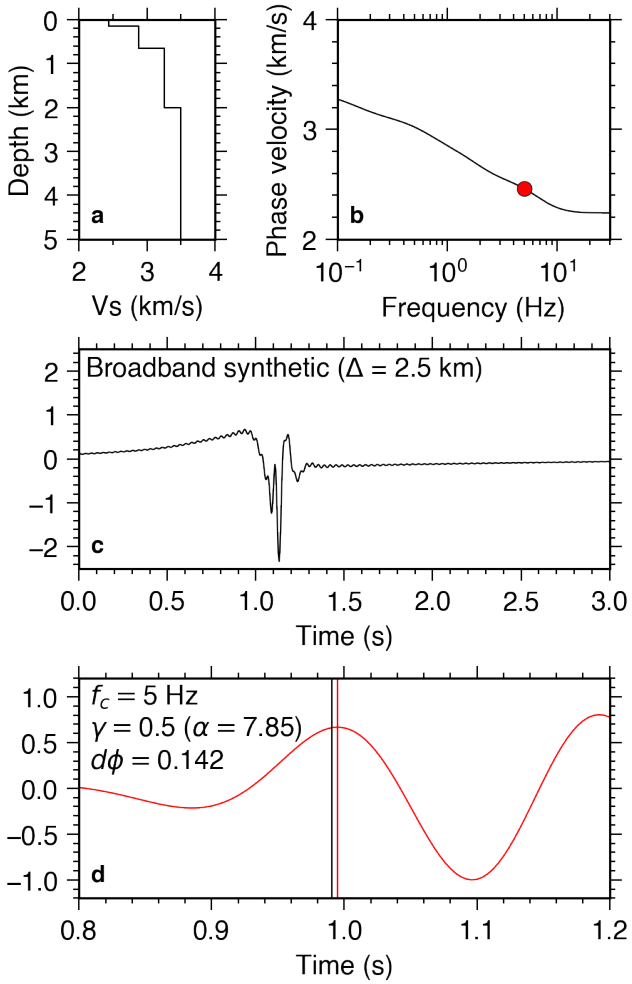

507

508 **Figure 6**. Example of the evaluation of the finite-frequency phase shift using a simplified model of the
509 Dublin Basin. (a) The velocity model (only the top 5 km portion of the shear-wave velocity model is
510 shown); (b) Rayleigh wave phase velocity dispersion curve. The red dot denotes the frequency (5 Hz) used
511 in panel d; (c) Broadband synthetic of the noise cross-correlation function at the interstation distance of 2.5
512 km; (d) Filtered waveform. The Gaussian filter is centered at 5 Hz, with γ = 0.5, or α = 7.85. The finite-
513 frequency phase shift is 0.142 radians. We used a smaller γ for a clearer illustration of the phase shift.

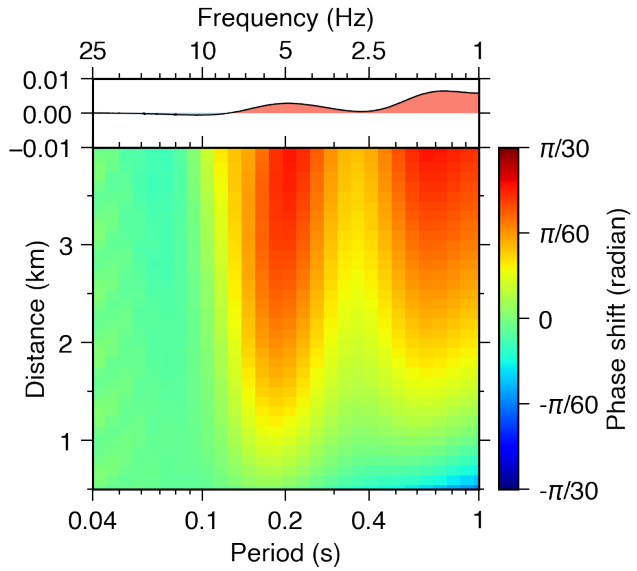

514

515 **Figure 7**. Phase shift (bottom) and the second derivative of $k(\omega)$ (top). (Top) The red shaded region marks
516 the positive $k''(\omega)$; (Bottom) The positive phase shift indicates phase delay; the negative phase shift—phase
517 advance.

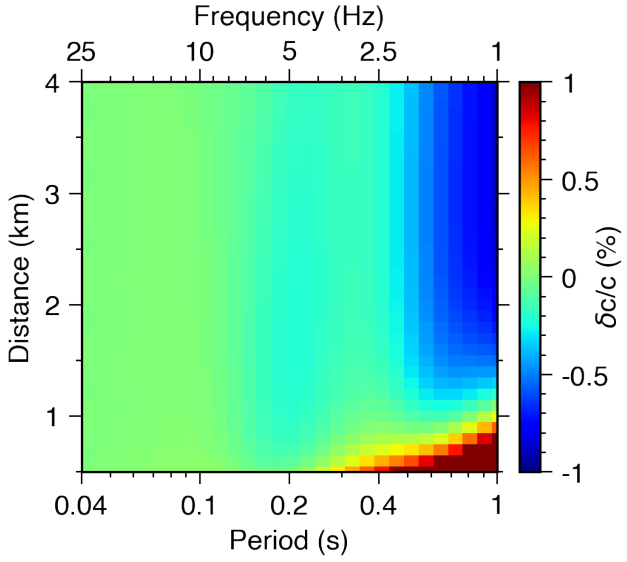

518

519 **Figure 8**. Phase velocity perturbation corresponding to the phase shift in Figure 7. The perturbation is with
520 respect to the phase velocity dispersion curve that is used to generate the synthetics.

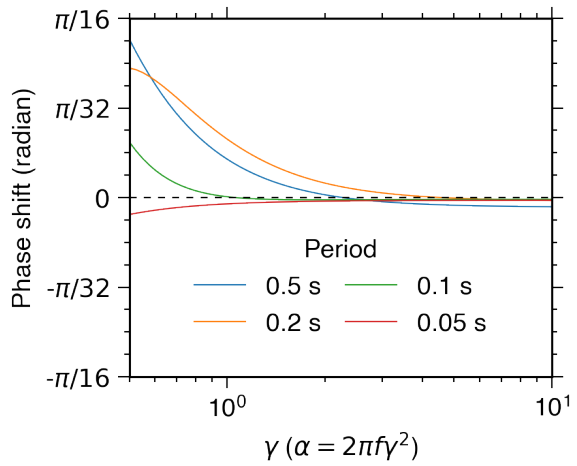

Figure 9. Phase shift as a function of γ. We compute the example using an interstation distance of 2.5 km and Gaussian filtered centered at 2 Hz, 5 Hz, 10 Hz and 20 Hz.

4.2 Long-period example

The phase shift can be observed in long-period measurements as well. In this example, we use the phase velocity dispersion curve computed for the global reference model ak135. The phase shifts computed here illustrate the errors that can be incurred in long-period measurements performed with time-domain methods, which are widely used for crustal and lithospheric imaging. We also discuss a technique—ridge jumping—that can improve the quality of measurements, especially at shorter periods.

We evaluated the finite-frequency phase shift within the distance range of 100-3000 km (every 100 km) and the period range of 25-100 s. The broadband synthetic was computed by integrating over 2-50 mHz with an interval of 0.01 mHz, and the width of the Gaussian filters was set to γ = 16 (Soomro et al., 2016). We adopted the ridge jumping technique (Bonadio et al., 2018; T. Meier et al., 2004; Soomro et al., 2016; Xu et al., 2021), selecting high-amplitude ridges when scanning from low to high frequency, rather than staying on one ridge for the entire frequency band (Figure

10a). For the stability of the results, we only jump to the adjacent ridges and do so only when their amplitude is 1.5 times higher than that of the current ridge (Xu et al., 2021). The ridge jumping may produce discontinuities in the observed phase shift (Figure 10b), but it can reduce the phase shift at higher frequencies (> 0.03 Hz).

The phase shift for the model ak135 ranges from $-\pi/44$ to $\pi/16$, if we use multiple ridges (Figure 10d). This is ~18 times smaller than the values obtained when using the single, 0th ridge ($-3\pi/2$ to $\pi/40$; Figure 10c). The corresponding velocity perturbation is up to 0.2% at interstation or source-station distances above 300 km (Figure 11). Below 300 km, the near-field effect becomes dominant and increases the perturbation to 0.9%.

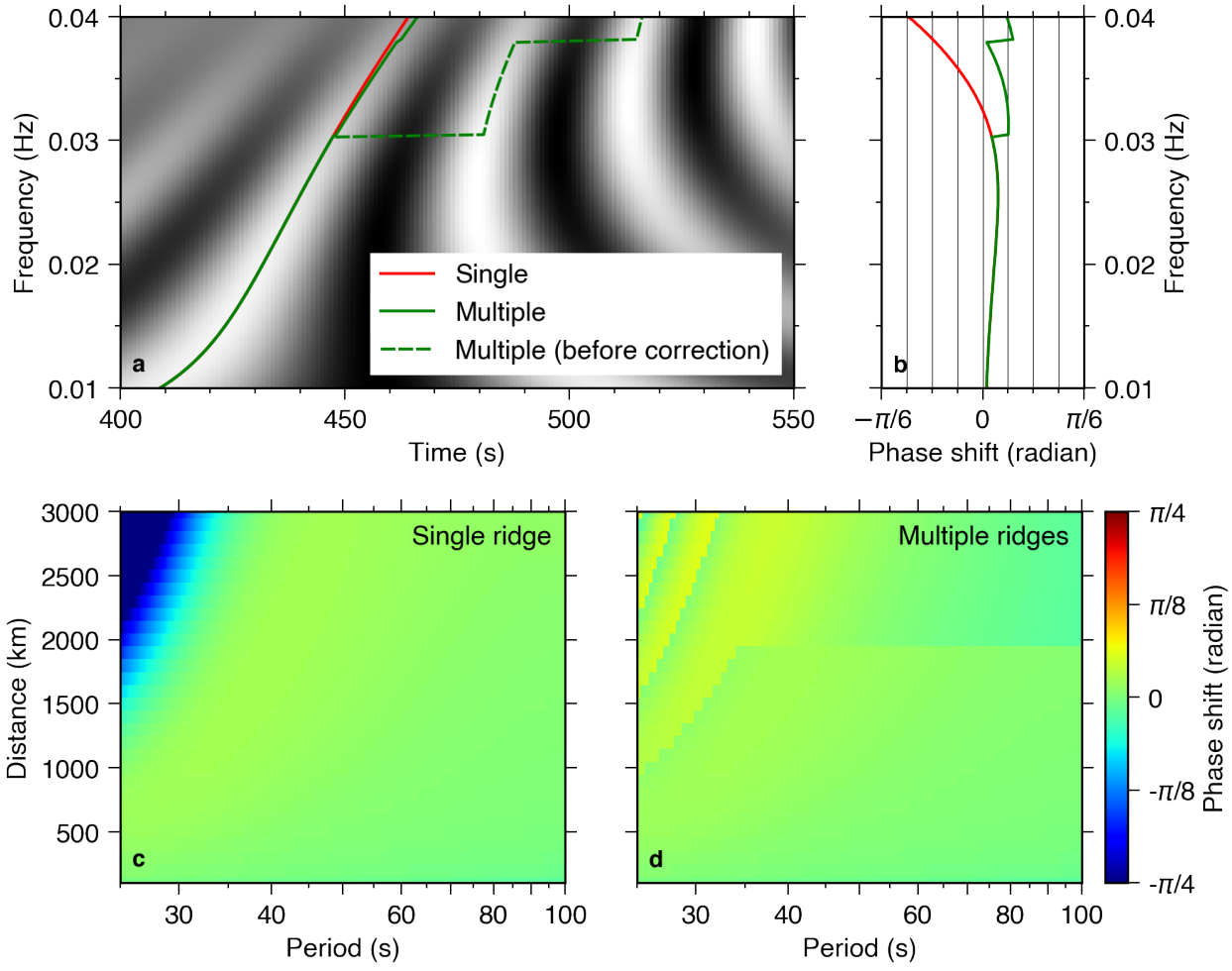

547 **Figure 10**. Phase shift in the measurements made on synthetic traces computed for ak135. (a) Frequency-
548 time representation of the synthetic surface wave at 1750 km. Red and green solid lines denote the phase
549 travel time measured using single ridge and multiple ridges, respectively. The green dashed line marks the
550 ridge picked by the ridge jumping method. (b) Phase shift computed using the single-ridge and multiple-
551 ridge phase travel time at the distance of 1750 km. (c) Phase shift computed using single ridges at the
552 distance range of 100-3000 km. (d) Same as c, but using the ridge jumping method.

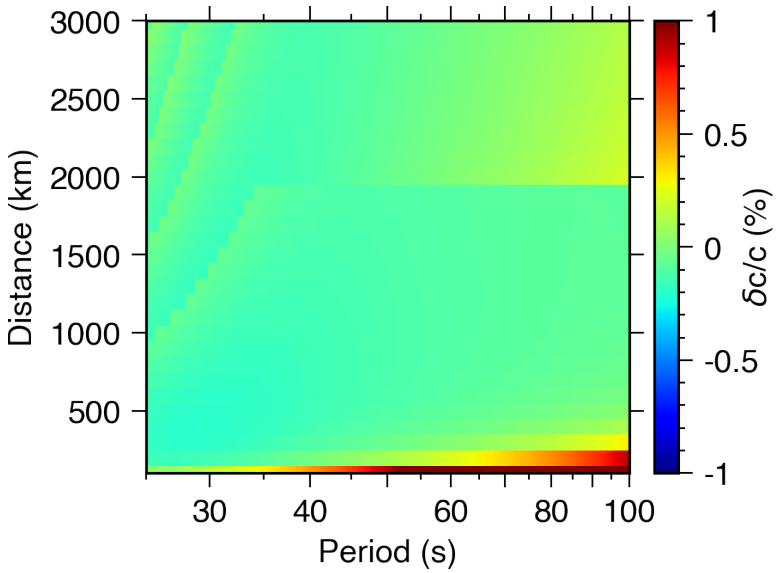

553

554 **Figure 11**. Phase velocity perturbations corresponding to the phase shifts shown in Figure 10.

555 **5 Discussion**

556 Using the calculations above, we found that the finite-frequency phase shift is relatively small
557 in the range of distance, frequency and γ that are commonly used in the surface wave studies. It
558 can be large, however, at (1) long distance, (2) high frequencies, (3) with relatively wide-band
559 filters or (4) rapid changes with frequency in the group velocity curve. In terms of phase velocity
560 perturbations, their dependences on the distance and frequency cancel out, so that only the
561 bandwidth of the filters and the rate of group-velocity change—or, equivalently, $k''(\omega)$—have a

562 significant effect. We can tune the bandwidth of the filters, but $k''(\omega)$ is determined by the Earth's
563 structure.

564 We also observed another type of phase shift, in addition to the finite-frequency phase shift.
565 This phase shift dominates in the near field and is discussed below. We also discuss whether the
566 finite-frequency phase shift exists in the frequency-domain method.

567 5.1 The near-field phase shift

568 The phase shift computed using the Dublin Basin model is negative at 1 Hz around the
569 distance of 0.5 km, in contrast to the positive phase shift at the same frequency but longer distances
570 ($\Delta > 1$ km). Furthermore, it is seemingly inconsistent with the positive $k''(\omega)$ at 1 Hz. The
571 inconsistency is caused by a different type of phase shift, which we refer to as the near-field phase
572 shift. The near-field phase shift arises from the far-field approximation, assumed when Bessel
573 functions are replaced by cosine functions to represent monochromatic surface waves.

574 The phase shift computed by the numerical method described in Section 4 is the phase
575 difference between the monochromatic cosine functions and narrowband Bessel functions. It
576 comprises both the finite-frequency phase shift caused by the difference between monochromatic
577 Bessel functions and narrowband Bessel functions and the near-field phase shift caused by the
578 difference between monochromatic cosine functions and monochromatic Bessel functions.

579 We separated the two types of phase shift in Figure 12. In the isolated finite-frequency phase
580 shift, the negative anomaly no longer exists in the near-field corner, which is more consistent with
581 the prediction by equation 27 (Figure 12b). By contrast, the near-field phase shift is consistently
582 negative and only visible in the near field (Figure 12c), which can be predicted by

583 $$\delta\phi_{near} = -\arg H_0^{(2)}\left(\frac{\omega\Delta}{c}\right) - \left(\frac{\omega\Delta}{c} - \frac{\pi}{4}\right) \quad (33)$$

584 The phase of $H_0^{(2)}\left(\frac{\omega\Delta}{c}\right)$ should be unwrapped to obtain a continuous phase, which approaches -

585 $\omega\Delta/c + \pi/4$ at high frequencies, decreasing $\delta\phi_{near}$ to zero.

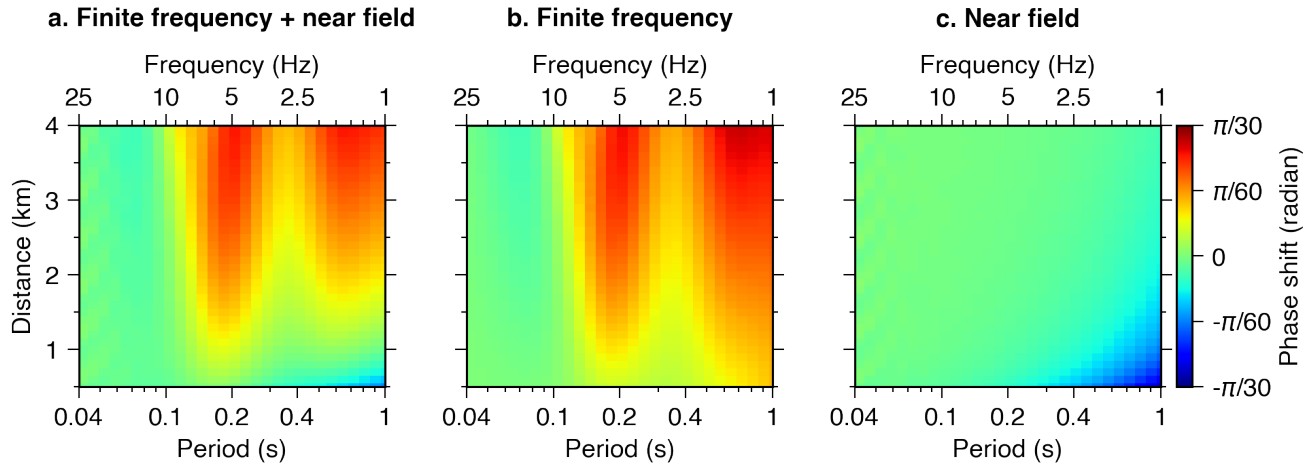

586

587 **Figure 12**. The origins of the finite-frequency and near-field phase shifts. The frames show the phase
588 differences (a) between narrow-band Bessel functions and monochromatic cosine functions; (b) between
589 narrow-band and monochromatic Bessel functions; (c) between monochromatic Bessel functions and
590 monochromatic cosine functions. The phase of monochromatic cosine functions is $\omega/\Delta - \pi/4$. The phase of
591 narrow-band ones is measured using synthetics.

592 ## 5.2 Time-domain method vs frequency-domain method

593 The finite-frequency phase shift only applies to measurement methods that use narrow-band
594 waveforms to measure the phase travel time in the time domain. Frequency-domain methods (e.g.,
595 phase unwrapping method; T. Meier et al., 2004) do not have such phase shift. The difference
596 between the two methods is that the phase unwrapping method measures the phase of the spectrum
597 at the center frequency, so that its results are monochromatic measurements, instead of narrow-

band measurements. The measured phase is then unwrapped, converted to the phase travel time, and compared to the predicted phase travel time as in the time domain method.

Figure 13 shows a comparison of the phase shift associated with the time domain method and the phase unwrapping method. We can see that the phase shift associated with the frequency domain method is at constant values for different γ. These constant values are not zero, which reflects the near-field phase shift.

The frequency-domain method is an attractive alternative to time-domain ones as it is free of the finite-frequency phase shift. The time-domain methods, however, remain very popular due to their simplicity. We note that the near-field phase shift is present regardless of the approach chosen.

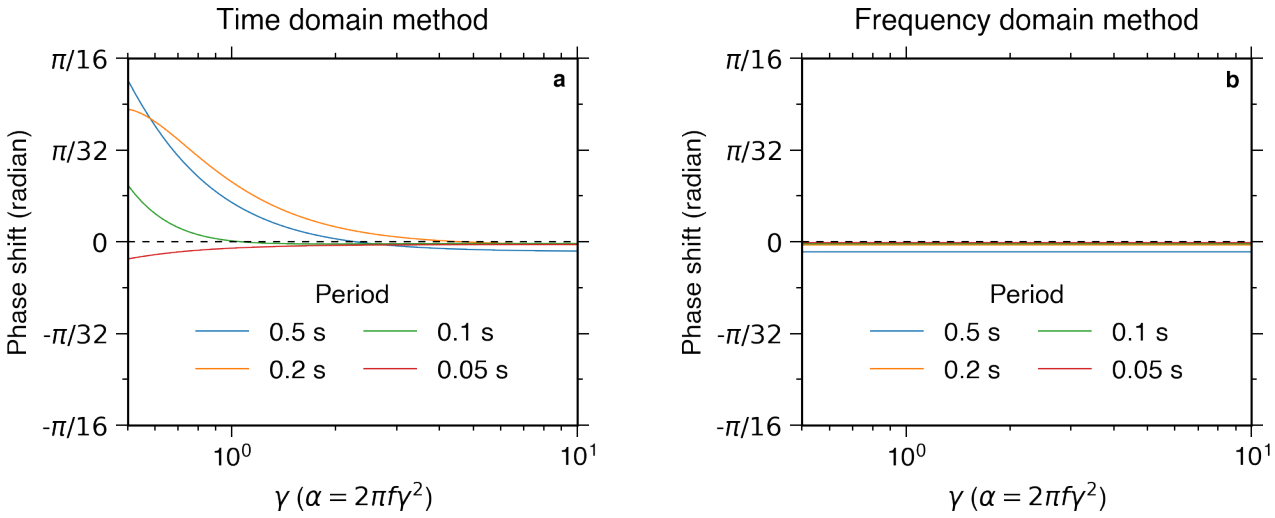

Figure 13. Phase shift as a function of γ for (a) the time-domain method and (b) the frequency-domain method.

6 Conclusions

The finite-frequency phase shift arises in the phase velocity measurements obtained using the time-domain methods due to the approximation of the monochromatic surface waves by narrow-band surface waves. It applies to both ambient noise studies and those using ballistic surface waves from earthquakes or active sources. The phase shift biases the measured phase travel time and, hence, the measured phase velocity. The finite-frequency phase shift can be up to $\pi/4$ when using a very broadband filter and down to nearly zero when using a very narrowband filter. The exact amount depends on four factors: (1) the second derivative of the wavenumber k with respect to ω; (2) the width of the filter; (3) the distance; (4) the center frequency of the Gaussian filter. For common settings in surface wave studies, the phase shift is about $\pi/60$-$\pi/16$, much smaller than the polar phase shift (phase advance of $\pi/2$) and source phase shift, identified previously (phase delay of $\pi/4$).

The finite-frequency phase shift can cause non-negligible phase-velocity perturbations of around 0.2% in long-period (25-100 s) studies and around 0.8% in high-frequency (1-25 Hz) studies. The exact amount can vary depending on the filter parameters and local Earth structure. If the acceptable level of errors in the phase velocity measurements is comparable to or lower than the finite-frequency phase shift, the shift should be corrected.

The finite-frequency phase shift, and its corresponding perturbation in phase velocities, can be corrected once having an estimation of the phase shift. A dispersion curve, computed from the 1-D velocity model inverted from an average dispersion curve or from the entire dataset of dispersion curves, can be used to compute a good estimation of the phase shift. It can be done by comparing the measured phase travel time in surface wave synthetics generated by the dispersion

curve to the far-field prediction of the phase travel time. The approach can also correct the near-field phase shift when using Bessel functions instead of cosine functions in generating synthetics.

Because the finite-frequency phase shift results from the monochromatic approximation, it does not exist in the frequency-domain methods that do not rely on the approximation. In this sense, switching to frequency-domain methods is an alternative approach for increasing the accuracy of phase-velocity measurements.

Acknowledgments

The work was supported by the European Union's Horizon 2020 research and innovation program under grant agreement No, 776622, PACIFIC , with additional support from the School of Physical Sciences, University of Cambridge. Figures were prepared with the Matplotlib package (Hunter, 2007). The velocity models used in the paper and codes for computing the finite-frequency phase shift and reproducing some of the figures in this paper are publicly available (Xu, 2021; doi: 10.5281/zenodo.5718901).

References

Aggelis, D. G., Kordatos, E. Z., Soulioti, D. V., & Matikas, T. E. (2010). Combined use of thermography and ultrasound for the characterization of subsurface cracks in concrete. *Construction and Building Materials, 24*(10), 1888–1897. https://doi.org/10.1016/j.conbuildmat.2010.04.014

Agius, M. R., & Lebedev, S. (2014). Shear-velocity structure, radial anisotropy and dynamics of the Tibetan crust. *Geophysical Journal International, 199*(3), 1395-1415. https://doi.org/10.1093/gji/ggu326

Agius, M. R., & Lebedev, S. (2017). Complex, multilayered azimuthal anisotropy beneath Tibet: evidence for co-existing channel flow and pure-shear crustal thickening. *Geophysical Journal International, 210*(3), 1823-1844. https://doi.org/10.1093/gji/ggx266

655 Aki, K. (1957). Space and time spectra of stationary waves with special reference to microtremors, *Bulletin of the*
656 *Earthquake Research Institute, 35,* 415-456.

657 Aki, K., & Richards, P. G. (2002). *Quantitative Seismology*. Sausalito, CA: University Science Books.

658 Bartzsch, S., Lebedev, S., & Meier, T. (2011). Resolving the lithosphere-asthenosphere boundary with seismic
659 Rayleigh waves, *Geophysical Journal International, 186(3)*, 1152–1164. https://doi.org/10.1111/j.1365-
660 246X.2011.05096.x

661 Beghein, C., Xing, Z., & Goes, S. (2019). Thermal nature and resolution of the lithosphere–asthenosphere boundary
662 under the Pacific from surface waves. *Geophysical Journal International, 216*(2), 1441-1465.
663 https://doi.org/10.1093/gji/ggy490

664 Bellefleur, G., Schetselaar, E., White, D., Miah, K., & Dueck, P. (2015). 3D seismic imaging of the Lalor
665 volcanogenic massive sulphide deposit, Manitoba, Canada. *Geophysical Prospecting*, *63*(4), 813–832.
666 https://doi.org/10.1111/1365-2478.12236

667 Bensen, G. D., Ritzwoller, M. H., Barmin, M. P., Levshin, A. L., Lin, F., Moschetti, M. P., Shapiro, N. M., & Yang,
668 Y. (2007). Processing seismic ambient noise data to obtain reliable broad-band surface wave dispersion
669 measurements. *Geophysical Journal International*, *169*(3), 1239–1260. https://doi.org/10.1111/j.1365-
670 246X.2007.03374.x

671 Bodet, L., van Wijk, K., Bitri, A., Abraham, O., Côte, P., Grandjean, G., & Leparoux, D. (2005). Surface-wave
672 inversion limitations from laser-Doppler physical modeling. *Journal of Environmental & Engineering*
673 *Geophysics, 10*(2), 151-162. https://doi.org/10.2113/JEEG10.2.151

674 Bonadio, R. (2019). Broadband surface wave tomography of Ireland, Britain, and Other Regions (Doctoral
675 dissertation). Dublin, Ireland: Trinity College Dublin.

676 Bonadio, R., Geissler, W. H., Lebedev, S., Fullea, J., Ravenna, M., Celli, N. L., Jokat, W., Jegen, M., Sens-
677 Schönfelder, C., & Baba, K. (2018). Hot upper mantle beneath the Tristan da Cunha Hotspot from
678 probabilistic Rayleigh-wave inversion and petrological modeling. *Geochemistry, Geophysics, Geosystems*,
679 *19*(5), 1412–1428. https://doi.org/10.1002/2017GC007347

680 Bourjot, L., & Romanowicz, B. (1992). Crust and upper mantle tomography in Tibet using surface waves.
681 *Geophysical Research Letters, 19*(9), 881-884. https://doi.org/10.1029/92GL00261

682 Brenguier, F., Shapiro, N. M., Campillo, M., Nercessian, A., & Ferrazzini, V. (2007). 3-D surface wave tomography
683 of the Piton de la Fournaise volcano using seismic noise correlations. *Geophysical Research Letters*, *34*,
684 L02305. https://doi.org/10.1029/2006GL028586

685 Brocher, T. M. (2005). Empirical relations between elastic wavespeeds and density in the Earth's crust. *Bulletin of*
686 *the Seismological Society of America*, *95*(6), 2081–2092. https://doi.org/10.1785/0120050077

687 Brune, J. N., Nafe, J. E., & Alsop, L. E. (1961). The polar phase shift of surface waves on a sphere. *Bulletin of the*
688 *Seismological Society of America*, *51*(2), 247–257. https://doi.org/10.1785/BSSA0510020247

689 Burgos, G., Montagner, J. P., Beucler, E., Capdeville, Y., Mocquet, A., & Drilleau, M. (2014). Oceanic lithosphere-
690 asthenosphere boundary from surface wave dispersion data. *Journal of Geophysical Research: Solid Earth,*
691 *119*(2), 1079-1093. https://doi.org/10.1002/2013JB010528

692 Dahlen, F. A., & Tromp, J. (1998). *Theoretical Global Seismology*. Princeton, NJ: Princeton University Press.

693 Dahlen, F. A., & Zhou, Y. (2006). Surface-wave group-delay and attenuation kernels, *Geophysical Journal*
694 *International*, *165*(2), 545–554. https://doi.org/10.1111/j.1365-246X.2006.02913.x

695 Delorey, A. A., & Vidale, J. E. (2011). Basin shear-wave velocities beneath Seattle, Washington, from noise-
696 correlation Rayleigh waves. *Bulletin of the Seismological Society of America*, *101*(5), 2162–2175.
697 https://doi.org/10.1785/0120100260

698 Deschamps, F., Lebedev, S., Meier, T., & Trampert, J. (2008). Stratified seismic anisotropy reveals past and present
699 deformation beneath the East-central United States. *Earth and Planetary Science Letters, 274*(3-4), 489-
700 498. https://doi.org/10.1016/j.epsl.2008.07.058

701 Dziewonski, A., & Bloch, S. (1972). Residual dispersion measurement—A new method of surface wave analysis.
702 *Bulletin of the Seismological Society of America*, *62*(1), 129–139.

703 Dziewonski, A., Bloch, S., & Landisman, M. (1969). A technique for the analysis of transient seismic signals.
704 *Bulletin of the Seismological Society of America*, *59*(1), 427–444.

Ekström, G. (2014). Love and Rayleigh phase-velocity maps, 5–40 s, of the western and central USA from USArray data. *Earth and Planetary Science Letters*, *402*, 42–49. https://doi.org/10.1016/j.epsl.2013.11.022

Ekström, G., Abers, G. A., & Webb, S. C. (2009). Determination of surface-wave phase velocities across USArray from noise and Aki's spectral formulation. *Geophysical Research Letters*, *36*(18), L18301. https://doi.org/10.1029/2009GL039131

Ekström, G., & Dziewonski, A. M. (1998). The unique anisotropy of the Pacific upper mantle. *Nature, 394*(6689), 168-172. https://doi.org/10.1038/28148

El-Sharkawy, A., Meier, T., Lebedev, S., Behrmann, J.H., Hamada, M., Cristiano, L., Weidle, C., & Köhn, D. (2020). The slab puzzle of the Alpine-Mediterranean region: Insights from a new, high-resolution, shear wave velocity model of the upper mantle. *Geochemistry, Geophysics, Geosystems, 21*(8), e2020GC008993. https://doi.org/10.1029/2020GC008993

Fry, B., Deschamps, F., Kissling, E., Stehly, L., & Giardini, D. (2010). Layered azimuthal anisotropy of Rayleigh wave phase velocities in the European Alpine lithosphere inferred from ambient noise. *Earth and Planetary Science Letters*, *297*(1–2), 95–102. https://doi.org/10.1016/j.epsl.2010.06.008

Gradshteyn, I. S., & Ryzhik, I. M. (2014). *Table of integrals, series and products*. San Diego, CA: Academic Press.

Herrmann, R. B. (1973). Some aspects of band-pass filtering of surface waves. *Bulletin of the Seismological Society of America*, *63*(2), 663–671.

Herrmann, R. B. (2013). Computer programs in seismology: An evolving tool for instruction and research, *Seismological Research Letters, 84*, 1081-1088. https://doi.org/10.1785/0220110096.

Hollis, D., Mcbride, J., Beaupretre, S., Mordret, A., Brenguier, F., Arndt, N., & Good, D. (2019). Ambient noise surface wave tomography at the Marathon PGM-Cu deposit, Ontario, Canada. *Recorder*, *44*(4), 1–20.

Hunter, J. D. (2007). Matplotlib: A 2D graphics environment. *Computing in Science & Engineering*, *9*(3), 90–95. https://doi.org/10.1109/MCSE.2007.55

728 Inzunza, D. A., Montalva, G. A., Leyton, F., Prieto, G. A., & Ruiz, S. (2019). Shallow ambient-noise 3D
729 tomography in the Concepción Basin, Chile: Implications for low-frequency ground motions. *Bulletin of*
730 *the Seismological Society of America*, *109*(1), 75–86. https://doi.org/10.1785/0120180061

731 Kästle, E. D., Soomro, R., Weemstra, C., Boschi, L., & Meier, T. (2016). Two-receiver measurements of phase
732 velocity: Cross-validation of ambient-noise and earthquake-based observations. *Geophysical Journal*
733 *International*, *207*(3), 1493–1512. https://doi.org/10.1093/gji/ggw341

734 Kennett, B. L. N., Engdahl, E. R., & Buland, R. (1995). Constraints on seismic velocities in the Earth from
735 traveltimes. *Geophysical Journal International*, *122*(1), 108–124. https://doi.org/10.1111/j.1365-
736 246X.1995.tb03540.x

737 Kolínský, P., Bokelmann, G., & the AlpArray Working Group. (2019). Arrival angles of teleseismic fundamental
738 mode Rayleigh waves across the AlpArray. *Geophysical Journal International, 218*(1), 115–144.
739 https://doi.org/10.1093/gji/ggz081

740 Lebedev, S., Adam, J. M.-C., & Meier, T. (2013). Mapping the Moho with seismic surface waves: A review,
741 resolution analysis, and recommended inversion strategies. *Tectonophysics*, *609*, 377–394.
742 https://doi.org/10.1016/j.tecto.2012.12.030

743 Levshin, A., & Ratnikova, L. (1984). Apparent ansiotropy in inhomogeneous media. *Geophysical Journal*
744 *International, 76*(1), 65-69. https://doi.org/10.1111/j.1365-246X.1984.tb05022.x

745 Levshin, A., Ratnikova, L., & Berger, J. (1992). Peculiarities of surface-wave propagation across central Eurasia.
746 *Bulletin of the Seismological Society of America*, *82*(6), 2464–2493.

747 Li, C., Yao, H., Fang, H., Huang, X., Wan, K., Zhang, H., & Wang, K. (2016). 3D near-surface shear-wave velocity
748 structure from ambient-noise tomography and borehole data in the Hefei urban area, China. *Seismological*
749 *Research Letters*, *87*(4), 882–892. https://doi.org/10.1785/0220150257

750 Licciardi, A., & Piana Agostinetti, N. (2017). Sedimentary basin exploration with receiver functions: Seismic
751 structure and anisotropy of the Dublin Basin (Ireland). *Geophysics*, *82*(4), KS41–KS55.
752 https://doi.org/10.1190/geo2016-0471.1

753 Lindner, F., Laske, G., Walter, F., & Doran, A. K. (2019). Crevasse-induced Rayleigh-wave azimuthal anisotropy
754 on Glacier de la Plaine Morte, Switzerland. *Annals of Glaciology*, *60*(79), 96–111.
755 https://doi.org/10.1017/aog.2018.25

756 Luo, Y., Yang, Y., Xu, Y., Xu, H., Zhao, K., & Wang, K. (2015). On the limitations of interstation distances in
757 ambient noise tomography. *Geophysical Journal International*, *201*(2), 652–661.
758 https://doi.org/10.1093/gji/ggv043

759 Martins, J. E., Ruigrok, E., Draganov, D., Hooper, A., Hanssen, R. F., White, R. S., & Soosalu, H. (2019). Imaging
760 Torfajökull's magmatic plumbing system with seismic interferometry and phase velocity surface wave
761 tomography. *Journal of Geophysical Research: Solid Earth*, *124*(3), 2920–2940.
762 https://doi.org/10.1029/2018JB016002

763 Masters, T.G., Johnson, S., Laske, G., & Bolton, H. (1996). A shear-velocity model of the mantle. *Philosophical*
764 *Transactions of the Royal Society of London. Series A: Mathematical, Physical and Engineering Sciences,*
765 *354*(1711), 1385-1411. https://doi.org/10.1098/rsta.1996.0054

766 Meier, T., Dietrich, K., Stöckhert, B., & Harjes, H.-P. (2004). One-dimensional models of shear wave velocity for
767 the eastern Mediterranean obtained from the inversion of Rayleigh wave phase velocities and tectonic
768 implications. *Geophysical Journal International*, *156*(1), 45–58. https://doi.org/10.1111/j.1365-
769 246X.2004.02121.x

770 Meier, T., Auras, M., Fehr, M., Köhn, D., Cristiano, L., Sobott, R., Mosca, I., Ettl, H., Eckel, F., Steinkraus, T.,
771 Erkul, E., Schulte-Kortnack, D., Sigloch, K., Bilgili, F., Gioia, E. D., & Presicce C. P. (2017). Investigating
772 surficial alterations of natural stone by ultrasonic surface measurements. In N. Masini & F. Soldovieri
773 (Eds.), *Sensing the Past: From artifact to historical site* (pp. 257-288). Cham, Switzerland: Springer
774 International Publishing.

775 Meier, U., Curtis, A., & Trampert, J. (2007). Global crustal thickness from neural network inversion of surface wave
776 data. *Geophysical Journal International, 169*(2), 706-722. https://doi.org/10.1111/j.1365-
777 246X.2007.03373.x

778 Mi, B., Xia, J., Bradford, J. H., & Shen, C. (2020). Estimating near-surface shear-wave-velocity structures via
779 multichannel analysis of Rayleigh and love waves: An experiment at the Boise hydrogeophysical research
780 site. *Surveys in Geophysics, 41*(2), 323-341. https://doi.org/10.1007/s10712-019-09582-4

781 Molinari, I., Verbeke, J., Boschi, L., Kissling, E., & Morelli, A. (2015). Italian and Alpine three-dimensional crustal
782 structure imaged by ambient-noise surface-wave dispersion. *Geochemistry, Geophysics, Geosystems*,
783 *16*(12), 4405–4421. https://doi.org/10.1002/2015GC006176

784 Mordret, A., Landès, M., Shapiro, N. M., Singh, S. C., Roux, P., & Barkved, O. I. (2013). Near-surface study at the
785 Valhall oil field from ambient noise surface wave tomography. *Geophysical Journal International*, *193*(3),
786 1627–1643. https://doi.org/10.1093/gji/ggt061

787 Mordret, A., Roux, P., Boué, P., & Ben-Zion, Y. (2019). Shallow three-dimensional structure of the San Jacinto
788 fault zone revealed from ambient noise imaging with a dense seismic array. *Geophysical Journal*
789 *International*, *216*(2), 896–905. https://doi.org/10.1093/gji/ggy464

790 Moschetti, M. P., Ritzwoller, M. H., & Shapiro, N. M. (2007). Surface wave tomography of the western United
791 States from ambient seismic noise: Rayleigh wave group velocity maps. *Geochemistry, Geophysics,*
792 *Geosystems*, *8*(8), Q08010. https://doi.org/10.1029/2007GC001655

793 Nicolson, H., Curtis, A., & Baptie, B. (2014). Rayleigh wave tomography of the British Isles from ambient seismic
794 noise. *Geophysical Journal International*, *198*(2), 637–655. https://doi.org/10.1093/gji/ggu071

795 Pan, Y., Gao, L., & Bohlen, T. (2019). High-resolution characterization of near-surface structures by surface-wave
796 inversions: From dispersion curve to full waveform. *Surveys in Geophysics*, *40*(2), 167–195.
797 https://doi.org/10.1007/s10712-019-09508-0

798 Pasyanos, M. E., Masters, T. G., Laske, G., & Ma, Z. (2014). LITHO1. 0: An updated crust and lithospheric model
799 of the Earth. *Journal of Geophysical Research: Solid Earth, 119*(3), 2153-2173.
800 https://doi.org/10.1002/2013JB010626

801 Pawlak, A., Eaton, D. W., Darbyshire, F., Lebedev, S., & Bastow, I. D. (2012). Crustal anisotropy beneath Hudson
802 Bay from ambient noise tomography: evidence for post-orogenic lower-crustal flow?, *Journal of*
803 *Geophysical Research: Solid Earth, 117*(B8). https://doi.org/doi:10.1029/2011JB009066.

804 Polat, G., Lebedev, S., Readman, P. W., O'Reilly, B. M., & Hauser, F. (2012). Anisotropic Rayleigh-wave
805 tomography of Ireland's crust: Implications for crustal accretion and evolution within the Caledonian
806 Orogen. *Geophysical Research Letters, 39*(4). https://doi.org/10.1029/2012GL051014

807 Pollitz, F. F. (2001). Remarks on the travelling wave decomposition. *Geophysical Journal International, 144*(2),
808 233-246. https://doi.org/10.1046/j.1365-246x.2001.00271.x

809 Preiswerk, L. E., & Walter, F. (2018). High-frequency (>2 Hz) ambient seismic noise on high-melt glaciers: Green's
810 function estimation and source characterization. *Journal of Geophysical Research: Earth Surface*, *123*(8),
811 1667–1681. https://doi.org/10.1029/2017JF004498

812 Brilliant, R. M., & Ewing, M. (1954). Dispersion of Rayleigh waves across the U.S. *Bulletin of the Seismological*
813 *Society of America*, *44*(2A), 149–158. https://doi.org/10.1785/BSSA04402A0149

814 Ritzwoller, M. H., & Levshin, A. L. (1998). Eurasian surface wave tomography: Group velocities. *Journal of*
815 *Geophysical Research: Solid Earth*, *103*(B3), 4839–4878. https://doi.org/10.1029/97JB02622

816 Roux, P., Wathelet, M., & Roueff, A. (2011). The San Andreas Fault revisited through seismic-noise and surface-
817 wave tomography. *Geophysical Research Letters*, *38*(13), L13319. https://doi.org/10.1029/2011GL047811

818 Sabra, K. G., Gerstoft, P., Roux, P., Kuperman, W. A., & Fehler, M. C. (2005). Surface wave tomography from
819 microseisms in Southern California. *Geophysical Research Letters*, *32*(14), L14311.
820 https://doi.org/10.1029/2005GL023155

821 Schwab, F., & Kausel, E. (1976). Long-period surface wave seismology: Love wave phase velocity and polar phase
822 shift. *Geophysical Journal International*, *45*(2), 407–435. https://doi.org/10.1111/j.1365-
823 246X.1976.tb00334.x

824 Shapiro, N. M., Campillo, M., Stehly, L., & Ritzwoller, M. H. (2005). High-resolution surface-wave tomography
825 from ambient seismic noise. *Science*, *307*(5715), 1615–1618. https://doi.org/10.1126/science.1108339

826 Shapiro, N. M., & Ritzwoller, M. H. (2002). Monte-Carlo inversion for a global shear-velocity model of the crust
827 and upper mantle. *Geophysical Journal International, 151*(1), 88-105. https://doi.org/10.1046/j.1365-
828 246X.2002.01742.x

829 Shapiro, N. M., & Singh, S. (1999). A systematic error in estimating surface-wave group-velocity dispersion curves
830 and a procedure for its correction. *Bulletin of the Seismological Society of America*, *89*(4), 1138–1142.
831 https://doi.org/10.1785/BSSA0890041138

832 Socco, L. V., Foti, S., & Boiero, D. (2010). Surface-wave analysis for building near-surface velocity models—
833 Established approaches and new perspectives. *Geophysics, 75*(5), 75A83-75A102.
834 https://doi.org/10.1190/1.3479491

835 Soomro, R. A., Weidle, C., Cristiano, L., Lebedev, S., Meier, T., & PASSEQ Working Group. (2016). Phase
836 velocities of Rayleigh and Love waves in central and northern Europe from automated, broad-band,
837 interstation measurements. *Geophysical Journal International*, *204*(1), 517–534.
838 https://doi.org/10.1093/gji/ggv462

839 Toksöz, M. N., & Anderson, D. L. (1966). Phase velocities of long-period surface waves and structure of the upper
840 mantle: 1. Great-Circle Love and Rayleigh wave data. *Journal of Geophysical Research*, *71*(6), 1649–1658.
841 https://doi.org/10.1029/JZ071i006p01649

842 Tromp, J., & Dahlen, F. A. (1992). Variational principles for surface wave propagation on a laterally heterogeneous
843 Earth-II. Frequency-domain JWKB theory. *Geophysical Journal International*, *109*, 599–619.
844 https://doi.org/10.1111/j.1365-246x.1992.tb00120.x

845 Tromp, J., & Dahlen, F. A. (1993). Maslov theory for surface wave propagation on a laterally heterogeneous earth.
846 *Geophysical Journal International*, *115*(2), 512–528. https://doi.org/10.1111/j.1365-246X.1993.tb01203.x

847 Verbeke, J., Boschi, L., Stehly, L., Kissling, E., & Michelini, A. (2012). High-resolution Rayleigh-wave velocity
848 maps of central Europe from a dense ambient-noise data set. *Geophysical Journal International*, *188*(3),
849 1173–1187. https://doi.org/10.1111/j.1365-246X.2011.05308.x

850 Wang, Y., Lin, F.-C., Schmandt, B., & Farrell, J. (2017). Ambient noise tomography across Mount St. Helens using
851 a dense seismic array. *Journal of Geophysical Research: Solid Earth*, *122*(6), 4492–4508.
852 https://doi.org/10.1002/2016JB013769

853 Wang, Z., Dahlen, F. A., & Tromp, J. (1993). Surface wave caustics. *Geophysical Journal International*, *114*(2),
854 311–324. https://doi.org/10.1111/j.1365-246X.1993.tb03920.x

855 Wathelet, M., Jongmans, D., & Ohrnberger, M. (2004). Surface-wave inversion using a direct search algorithm and
856 its application to ambient vibration measurements. *Near Surface Geophysics, 2*(4), 211–221.
857 https://doi.org/10.3997/1873-0604.2004018

858 Wielandt, E. (1980). First-order asymptotic theory of the polar phase shift of Rayleigh waves. *Pure and Applied*
859 *Geophysics*, *118*, 1214–1227. https://doi.org/10.1007/BF01593062

860 Xia, J., Miller, R. D., & Park, C. B. (1999). Estimation of near-surface shear-wave velocity by inversion of Rayleigh
861 waves. *Geophysics*, *64*(3), 691–700. https://doi.org/10.1190/1.1444578

862 Xu, Y., Lebedev, S., Meier, T., Bonadio, R., & Bean, C. J. (2021). Optimized workflows for high-frequency seismic
863 interferometry using dense arrays. *Geophysical Journal International*, *227*(2), 875–897.
864 https://doi.org/10.1093/gji/ggab260

865 Xu, Y. (2021). blazing216/finite-frequency-phase-shift: November 22, 2021 Release (Version 1.0.1). Zenodo.
866 https://doi.org/10.5281/zenodo.5718901

867 Yao, H., van der Hilst, R. D., & de Hoop, M. V. (2006). Surface-wave array tomography in SE Tibet from ambient
868 seismic noise and two-station analysis—I. Phase velocity maps. *Geophysical Journal International*, *166*(2),
869 732–744. https://doi.org/10.1111/j.1365-246X.2006.03028.x

870 Zhan, Z., Tsai, V. C., Jackson, J. M., & Helmberger, D. (2014). Ambient noise correlation on the Amery Ice Shelf,
871 East Antarctica. *Geophysical Journal International*, *196*(3), 1796–1802. https://doi.org/10.1093/gji/ggt488

872 Zhang, X., Paulssen, H., Lebedev, S., & Meier, T. (2007). Surface wave tomography of the Gulf of California.
873 *Geophysical Research Letters, 34*(15). https://doi.org/10.1029/2007gl030631

874 Zhang, X., Paulssen, H., Lebedev, S., & Meier, T. (2009). 3D shear velocity structure beneath the Gulf of California
875 from Rayleigh wave dispersion, *Earth and Planetary Science Letters, 279*(3–4), 255–262.
876 https://doi.org/10.1016/j.epsl.2009.01.003